

Host, Viral, and Environmental Transcriptome Profiles of the Severe Acute Respiratory Syndrome Coronavirus 2 (SARS-CoV-2)

Authors:

Daniel J. Butler^{1#}, Christopher Mozsary^{1#}, Cem Meydan^{1,3,4#}, David Danko^{1,2#}, Jonathan Foox^{1,3#}, Joel Rosiene^{5,6}, Alon Shaiber^{5,6}, Ebrahim Afshinnkoo^{1,3,4}, Matthew MacKay¹, Fritz J. Sedlazeck⁷, Nikolay A. Ivanov^{1,3,8}, Maria Sierra¹, Diana Pohle¹³, Michael Zietz¹⁴, Vijendra Ramlall^{14,15}, Undina Gisladottir¹⁴, Craig D. Westover¹, Krista Ryon¹, Benjamin Young¹, Chandrima Bhattacharya¹, Phyllis Ruggiero⁶, Bradley W. Langhorst¹⁶, Nathan Tanner¹⁶, Justyna Gawrys⁶, Dmitry Meleshko^{1,2}, Dong Xu¹⁰, Jenny Xiang^{8,10}, Angelika Iftner¹³, Daniela Bezdán¹³, John Siple⁶, Lin Cong⁶, Arryn Craney⁶, Priya Velu⁶, Ari M. Melnick¹⁷, Iman Hajirasouliha^{1,3,18}, Thomas Iftner¹³, Mirella Salvatore⁹, Massimo Loda⁶, Lars F. Westblade^{6,9}, Shawn Levy¹¹, Melissa Cushing⁶, Nicholas Tatonetti¹⁴, Marcin Imielinski^{5,6*}, Hanna Rennert^{6*}, Christopher E. Mason^{1,3,5,12*}

Affiliations:

¹Department of Physiology and Biophysics, Weill Cornell Medicine, NY, USA.

²Tri-Institutional Computational Biol. & Medicine Program, Weill Cornell Medicine, NY, USA

³The HRH Prince Alwaleed Bin Talal Bin Abdulaziz Alsaud Institute for Computational Biomedicine, Weill Cornell Medicine, NY, USA

⁴WorldQuant Initiative for Quantitative Prediction, Weill Cornell Medicine, NY, USA

⁵New York Genome Center, NY, USA

⁶Department of Pathology and Laboratory Medicine, Weill Cornell Medicine, NY, USA

⁷Baylor College of Medicine, Houston, TX, USA

⁸Clinical & Translational Science Center, Weill Cornell Medicine, NY, USA

⁹Division of Infectious Diseases, Department of Medicine, Weill Cornell Medicine, NY, USA

¹⁰Genomics Resources Core Facility, Weill Cornell Medicine, NY, USA

¹¹HudsonAlpha Discovery Institute, Huntsville, AL, USA

¹²The Feil Family Brain and Mind Research Institute, Weill Cornell Medicine, NY, USA

¹³Institute of Medical Virology and Epidemiology of Viral Diseases, University Hospital Tuebingen, Germany

¹⁴Department of Biomedical Informatics, Department of Systems Biology, Department of Medicine, Institute for Genomic Medicine, Columbia University, NY, USA

¹⁵Department of Cellular and Molecular Physiology & Biophysics

¹⁶New England Biolabs, MA, USA

¹⁷Department of Medicine, Weill Cornell Medicine, NY, USA

¹⁸Englander Institute for Precision Medicine and the Meyer Cancer Center, Weill Cornell Medicine, NY, USA

#These authors contributed equally to this work

*To whom correspondence should be addressed

Corresponding Authors:

Marcin Imielinski (mai9037@med.cornell.edu); Hanna Rennert (har2006@med.cornell.edu); Christopher E. Mason (chm2042@med.cornell.edu) **Lead Contact:** chm2042@med.cornell.edu.

Abstract

The pandemic from the Severe Acute Respiratory Syndrome Coronavirus 2 (SARS-CoV-2) led to hundreds of thousands of deaths, including >15,000 in New York City (NYC). This pandemic highlighted a pressing clinical and public health need for rapid, scalable diagnostics that can detect SARS-CoV-2 infection, interrogate strain evolution, and map host response in patients. To address these challenges, we designed a fast (30 minute) colorimetric test to identify SARS-CoV-2 infection and simultaneously developed a large-scale shotgun metatranscriptomic profiling platform for nasopharyngeal swabs. Both technologies were used to profile 338 clinical specimens tested for SARS-CoV-2 and 86 NYC subway samples, creating a broad molecular picture of the COVID-19 epidemic in NYC. Our results nominate a novel, NYC-enriched SARS-CoV-2 subclade, reveal specific host responses in ACE pathways, and find medication risks associated with SARS-CoV-2 infection and ACE inhibitors. Our findings have immediate applications to SARS-CoV-2 diagnostics, public health monitoring, and therapeutic development.

Keywords: severe acute respiratory syndrome coronavirus 2 (SARS-CoV-2), coronavirus disease 2019 (COVID-19), loop-mediated isothermal amplification (LAMP), quantitative reverse transcription polymerase chain reaction (qRT-PCR), next-generation sequencing (NGS), RNA-seq, global health.

Introduction

In March 2020, the World Health Organization (WHO) declared a novel pandemic of the coronavirus disease 2019 (COVID-19), an infection caused by severe acute respiratory syndrome coronavirus 2 (SARS-CoV-2) (He *et al.*, 2020). Since then, New York City (NYC) has emerged as the global epicenter of this pandemic, with nearly one million cases and hundreds of thousands of deaths attributed to COVID-19 as of April 22, 2020, according to John's Hopkins University (JHU) Coronavirus Resource Center (<https://coronavirus.jhu.edu>).

The presenting symptoms of COVID-19 resemble those of common viral respiratory infections. As a result, molecular diagnosis is required to reliably distinguish SARS-CoV-2 infection from influenza and the agents of the common cold (Guan *et al.*, 2020, Zhou *et al.*, 2020). Current approaches to molecular testing are mostly limited to hospital laboratories and are largely reserved for the most severe cases, with limited accessibility to the general population. As a result, the prevalence of SARS-CoV-2 in the population is mostly unknown, particularly among mild or asymptomatic cases. Though several novel, scalable biotechnological innovations for viral testing have recently emerged (e.g., CRISPR-Cas12a (Broughton *et al.*, 2020) or CRISPR-Cas13 (Metsky *et al.*, 2020) on paper-based detection systems, or loop-mediated isothermal amplification (LAMP) (Tanner *et al.*, 2015, Zhang *et al.*, 2020, Yu *et al.*, 2020, Schmid-Burgk *et al.*, 2020) these have not been validated against gold-standard clinical assays or next-generation sequencing (NGS).

The lack of rapid and widely available SARS-CoV-2 diagnostics has fundamentally limited the public health approach to COVID-19, including the implementation of contact tracing and accurate estimation of infection fatality rates. In addition, the persistence of SARS-CoV-2 across a range of surfaces (e.g. glass, metal) for up to nine days in experimental conditions (van Doremalen *et al.*, 2020) and hospital areas (Ong *et al.*, 2020) raises the possibility that fomite

transmission may play a role in COVID-19 spread. A key question is whether the environmental surface distribution of SARS-CoV-2 in high-traffic areas (e.g. subways) may have driven its rapid emergence in certain regions (e.g., NYC).

Dynamic tracking of the evolution of the COVID-19 pandemic has been enabled by genomic viral surveillance resources such as Global Initiative on Sharing All Influenza Data (GISAID), the JHU Dashboard, and Nextstrain (<https://nextstrain.org/ncov>) (Gardy *et al.*, 2015, Dong *et al.*, 2020, Meyers *et al.*, 2020, Hadfield *et al.*, 2018). Nevertheless, the fraction of cases that have undergone full-length viral genome sequencing are still low (<0.5% of documented cases), underscoring the need for additional profiling, particularly in global infection epicenters such as NYC. Full-length viral genome sequences are required to track strain evolution, infer the temporal and geographic trajectories of spread, and correlate clinical features (e.g. disease severity, comorbidities, and viral load) with specific genotypes. Indeed, such genomic epidemiology efforts were crucial to confirm early community spread of SARS-CoV-2 in the U.S. States of Washington, California, and Connecticut (Zhao *et al.*, 2020, Gonzalez-Reiche *et al.*, 2020, Fauver *et al.*, 2020) as well as in China (Lu *et al.*, 2020). However current approaches to viral profiling (targeted sequencing of SARS-CoV-2) fail to provide information on host immune response or microbial co-infections, both which might modify presentation of COVID-19 and provide directions for therapeutic intervention.

To address these gaps in technology and disease knowledge, we designed and optimized a rapid LAMP assay to detect SARS-CoV-2 infection from nasopharyngeal swab specimens and oropharyngeal swab lysates. We then developed a large-scale shotgun metatranscriptomics platform to comprehensively profile nasopharyngeal swab samples collected from patients with total RNA sequencing (RNA-seq). Both technologies were applied to specimens from 338 confirmed or suspected COVID-19 patients at New York-Presbyterian Hospital-Weill Cornell Medical Center (NYPH-WCMC) and 86 environmental samples collected from high-transit areas in the NYC subway in early March 2020. Using these data, we validated the rapid LAMP assay against viral loads obtained with total RNA-seq and gold standard qPCR. We used full-length viral profiles to define a novel, NYC-enriched SARS-CoV-2 subclade. Finally, we integrated host and viral expression data with clinical metadata from NYPH-Columbia University Irving Medical Center (NYPH-CUIMC) to link perturbations in the angiotensin-converting enzyme pathway to SARS-CoV-2 viral loads and clinical outcomes. Our results propose novel molecular approaches for detecting and tracking SARS-CoV-2 infection, provide new molecular insights into the evolution of the COVID-19 outbreak in NYC, and implicate specific host factors and drug interactions in the biology of this disease.

Results

Rapid, single tube detection of SARS-CoV-2

We developed a colorimetric assay to quickly detect and quantify SARS-CoV-2 viral load in patient and environmental samples, utilizing a set of six LAMP primers and simple single tube protocol (**Figure 1b**). Primers were designed to create two nested loops and amplify within the SARS-CoV-2 nucleocapsid gene (N gene), which enabled a 30-minute reaction workflow. Related pathogens, high prevalence disease agents, and normal or pathogenic microbiota that are reasonably likely to be encountered in the clinical samples were evaluated to identify the percent

homology between the primer sequences and these other organisms, and the probes were also designed to avoid known polymorphisms (see Methods).

To validate the assay, we first evaluated two synthetic RNAs (see Methods) whose sequences matched the viral sequences of patients from Wuhan, China and Melbourne, Australia (**Supp. Fig. 1**). The first control (MT007544.1) was used to test the analytical sensitivity via the limit of detection (LoD), titrated from 1 million molecules of virus (10^6) down to a single copy, using serial log-10 dilutions. The reaction output was measured at 0-, 20-, and 30-minute intervals (**Figure 1c**, **Supp. Figure 2a**) before the samples were heated to 95°C for inactivation. The LoD was found to be between 10–100 viral total copies, and this was then replicated to show a similar LoD of 10–100 viral copies on the second synthetic control from the patient from Wuhan (**Supp. Figure 2b**).

We evaluated the reproducibility, clinical sensitivity, and clinical specificity of the LAMP assay across a set of serial titrations. Across these experiments, LAMP fluorescence correlated closely with SARS-CoV-2 RNA viral copies (**Figure 1d**), with an overlap of the median signal from negative controls at lower levels (25 total copies per reaction) of viral RNA ($n=10$). This translated to a 100% reproducibility at 1,000 and 500 total copies of viral RNA, 90% reproducibility at 100 copies, and 80% reproducibility at 50 copies (**Supp. Figure 3a**). This indicates an LoD threshold (95% reproducibility at two times the LoD) that is likely near 200 copies of RNA, with a maximum sensitivity of 10-50 copies of the viral RNA.

To optimize the LAMP assay for clinical samples, we first tested the reaction on a range of sample types, dilutions, and reaction volumes. We used a set of 201 COVID-19 samples that were tested for SARS-CoV-2 by qRT-PCR, including 69 nasopharyngeal (NP) swab samples that tested positive (clinical positives, qRT-PCR Ct<40) and 132 samples that tested negative (clinical negatives, qRT-PCR Ct \geq 40) (see Methods). Clinically positive samples showed a much higher fluorescence than negative samples, with superior performance observed with higher (10 μ L vs 5 μ L) input volumes (**Supp. Figure 3b**). Clinically positive samples that failed to generate LAMP fluorescence were associated with lower viral genome abundance (high cycle threshold [Ct] value qRT-PCR). We obtained similar performance on bulk oropharyngeal swab lysate (**Supp. Figure 3c-e**), including increasing reaction sensitivity as a function of viral copy number. This required only a 30-minute lysis time for the oral collections and 30-minute LAMP reaction time. These results indicate robust performance of the LAMP assay across a broad range of purified nucleic acids as well as crude cellular lysates (see Methods).

Having optimized the LAMP assay, we next evaluated its efficacy as a diagnostic across the 201 clinically-annotated samples. Quantitative LAMP fluorescence data were used to build a Receiver Operator Characteristic (ROC) plot and evaluate the clinical sensitivity and specificity of the assay. At the optimal threshold based on the reading from the Quantifluor relative fluorescence units (RFUs, 11,140), we observed an overall sensitivity of 95.6% and specificity of 99.4% (**Figure 1e**). With increasing viral load, as measured by qRT-PCR Ct values, the LAMP assay showed an increased diagnostic sensitivity (**Supp. Fig. 4**). The highest viral load (Ct <20) showed 100.0% sensitivity and 97.4% specificity, compared with the sensitivity at the lowest viral load at 80.0% (Ct >28, RFU below 7010). These same LAMP assay thresholds yielded consistent test positivity for synthetic RNA positive controls (Twist Biosciences) as well as

clinical spike-in carrier RNAs (20/20) (**Supp. Fig. 4**), and consistent signal from clinical viral positives in Vero 6 cells (100.0%, 12/12) and blank clinical buffer negatives (100.0% 8/8).

Shotgun metatranscriptomics platform for viral, microbiome, and host genomics

To provide orthogonal validation of our LAMP assay and further investigate the biological characteristics of clinical SARS-CoV-2 positive and negative samples, we developed a shotgun metatranscriptomics platform utilizing total RNA-seq (RNA-sequencing with ribosomal RNA depletion) to comprehensively profile human, microbial, fungal, and viral RNAs. We aligned total RNA-seq reads to several NCBI databases and classified those of non-human origin using Kraken2 (Wood *et al.*, 2019). Applying this platform to a full set of 338 COVID-19 specimens (including the 199 tested with LAMP), we obtained an average of 63.2M read pairs per total RNA-seq library.

The total RNA-seq data provided a broad view of the host transcriptome, the SARS-CoV-2 virus, as well as other domains of life. Libraries were dominated by reads that mapped to either human, bacterial, or SARS-CoV-2 genomes, in that order, but with lower proportion of reads mapping to fungi, archaea, or other viruses (**Figure 2c, 2d**). The reads that mapped to SARS-CoV-2 from total RNA-seq were sufficient to provide >10x coverage of the viral genomes for 118/132 (89.4%) of patient samples (**Figure 3a**), with robust (>1000X) sequencing depth of the genome for the high viral load (<Ct 25). Indeed, when downsampling the sets of reads/patient (50M down to 0.5M), we observed consistent detection of viral genomes and coverage across the entire viral genome in total RNA libraries from clinical positive samples (**Figure 3b**).

Clinical positive samples showed higher viral content (0.1%-62.2% of total RNA) than clinical negative samples (p-value < $2.2E^{-16}$, Wilcoxon rank-sum test). Comparing quantitative estimates of viral load from all three assays (LAMP, total-RNA Seq), we observed consistent profiles between the total RNA-seq viral abundance and the quantification by qRT-PCR and LAMP ($R_{seq_vs_Ct} = -0.84$, $R_{seq_vs_lamp} = 0.82$, $R_{lamp_vs_Ct} = -0.80$) (**Figure 2b, Supp. Figure 5**). Indeed, 97% of clinical negative samples (199/205) demonstrated fewer than 0.01% of total RNA-seq reads mapping to the SARS-CoV-2 reference. Three of the remaining six demonstrated high SARS-CoV-2 read proportion (>0.01%), high SARS-CoV-2 genome coverage (>99%), and high LAMP fluorescence, suggesting that these were qRT-PCR false negatives (**Supp. Figure 6**). The remaining three showed lower coverage (97%-99%) of the SARS-CoV-2 genome and low signal with LAMP. These data provide evidence that false negatives from qRT-PCR are likely rare (3-6/205, or 1.4-2.8%), but may require orthogonal assays to reliably detect.

Analysis of total RNA-seq sequences enabled mapping of co-infections and colonization with commensal species across both clinical positives and negatives in our sample set. We identified additional RNA viruses and organisms that distinguished high, medium, and lower viral load patients (**Supp Table 1**), with overall similarity observed across patients in the bacterial RNA fractions (**Supp. Figure 7a**). However, there were distinct variations in known respiratory viruses, including human coronaviruses 229E, NL63, and HKU1, as well as influenza A, rhinovirus (A and C), and respiratory syncytial virus (**Supp Figure 7a**). As expected, most patients (129/133) that presented with the SARS-CoV-2 virus lacked reads associated with other respiratory viruses. A subset of patients (4/133, 3.0%) also harbored Influenza A. These cases

were enriched in the lower titer (bottom third) of COVID-19 positive (3/4) patients. One patient carried SARS-CoV-2, human metapneumovirus, and coronavirus NL63 at the same time (**Supp Figure 7a,b**). These results indicate that a positive test for common respiratory viruses does not rule out the presence of SARS-CoV-2. There was also an associated depletion of several species of *Streptococcus*, *Veillonella*, and *Prevotella* in the high viral patient category (**Supp Figure 7c**) that was co-incident with SARS-CoV-2 infection, indicating a possible disruption of the host microbiome at the airway site of the NP swab collection.

Environmental sampling of SARS-CoV-2 in the NYC subway

Having validated a rapid LAMP assay and shotgun metatranscriptomics platform, we deployed both to investigate the environmental distribution of SARS-CoV-2 in high-transit areas of the NYC subway antecedent to the dawn of the NYC pandemic. We collected 86 samples from handrails, kiosks, and floors in Grand Central and Times Square subway stations between March 6 and 13th, 2020. Each sample was collected using a sterile and DNA/RNA free swab, following the MetaSUB sampling protocols for nucleic acid stabilization (Danko *et al.*, 2020). None of these 86 samples reached significant levels of LAMP fluorescence, suggesting that these high transit surfaces were likely free of SARS-CoV-2 virions.

To further investigate these 86 environmental samples for the presence of SARS-CoV-2, we generated total RNA-seq libraries and investigated the distribution of non-human sequences. These samples demonstrated a mix of fungal and archaeal species that was consistent with underground subway origin (Danko *et al.*, 2020) (**Supp. Table 1**). However, we did not observe significant counts or proportions (**Figure 2a**) of SARS-CoV-2 reads, which was particularly clear with dual-index library preparations (**Supp Figure 8**). However, a broad range of other bacterial and viral species was found, including a large set of phages (e.g. *Streptomyces* phage VWB), desiccation-tolerant bacteria (e.g. *Deinococcus radiodurans*), and more abundant bacterial and archaeal RNA than the clinical samples (**Supp. Table 1**). Of note, these were checked against a database of putative false positives (**Supp. Table 2**), which was created from *in silico* fragmentation of the SARS-CoV-2 genome and mapping against the same database. Taken together, these results indicate that high transit surfaces were not likely to harbor significant levels of SARS-CoV-2 in the early phases of the NYC epidemic.

Shotgun metatranscriptomes yield full-length SARS-CoV-2 genomes

We then investigated clinical samples with sufficient coverage across the 30kb SARS-CoV-2 genome (>10x) to identify genetic variants and place NYC strains onto phylogenetic tree of the global outbreak. We identified variants both through alignment and *de novo* assembly of Kraken-classified SARS-CoV-2 reads. In both cases, single nucleotide variants (SNVs) and indels (insertions/deletions) were called relative to the SARS-CoV-2 reference sequence (GCF_009858895.2) and then compared with 4,964 sequenced samples in GISAID (downloaded on 4/12/2020) using the Nextstrain database (Hadfield *et al.*, 2018).

Among our data, we found 692 instances of variants across 89 unique variant positions across the 93 samples with sufficient quality assemblies for placement into the Nextstrain-derived maximum likelihood phylogenetic tree (see methods). Though the vast majority (>80%) of variants were present across most (>99%) SARS-CoV-2 reads aligning to a given reference position, a small subset (7%) were polymorphic with robust read coverage (>=20 reads

supporting each allele and variant allele frequency 0.1-0.9), suggesting that microdiversity may play some role in SARS-CoV-2 evolution (**Figure 4**).

Analyzing groupings obtained from the Nextstrain-derived maximum likelihood phylogenetic tree, we found a high proportion (>83%) of our samples were associated with A2a, a large Western European derived clade that comprises nearly half of the sequences in GISAID. These results validate recently published findings (Gonzalez-Reiche *et al.*, 2020). In addition, we found additional samples from clades with mixed Asian and European sources (A1a, 7% of cases; B1, 3% of cases; B, 1% of cases; 4% of cases unassigned). Among these, we identified a clear predominance (90%) of the "L" strain, which is defined by a reference base at position 28143 (ORF8) and previously associated with severe cases in Wuhan (Tang *et al.*, 2020) (**Figure 4b**).

The only indel across the 89 genetic variants detected across our full-length assemblies was a 9 bp in-frame deletion (p.141_143KSD) in the gene encoding non-structural protein 1 (NSP1). NSP1 is a putative SARS-CoV-2 virulence factor that is highly divergent across betacoronaviruses (Narayanan *et al.*, 2015). This deletion was found via assembly in two of 93 NYPH-WCM samples, and showed robust read support with near 100% variant allele fraction across hundreds of high-quality alignments (**Figure 4c**). An identical deletion was observed in 14 other samples in the GISAID database, spanning samples from England, Iceland, and Canada. This included 12 samples that were labeled as part of clade A2a by Nextstrain (**Figure 4c**). This deletion removes three amino acids, including a variant position (143Y>F) in comparison to the SARS-CoV genome (**Figure 4d**). These residues occur in a conserved portion of the C-terminal region of NSP1, which has been linked to host chemokine dysregulation and translational inhibition in SARS-CoV (Narayanan *et al.*, 2015).

A novel SARS-CoV-2 subclade enriched in NYC case

Given the predominance of clade A2a among NYC cases (in our data and previous studies), we asked whether specific variants were enriched in NYC A2a samples relative to A2a samples from other regions. Comparing variant frequencies between A2a cases in our data and non-NYC cases in GISAID, we identified six enriched loci with FDR<0.1 (Fisher's exact test, one-tailed) that were over-represented in NYC A2a samples (**Figure 5a**). All six of these variants were significantly enriched (Bonferroni-adjusted p-value <0.05) in a second analysis comparing A2a GISAID cases from NYC vs. the rest of the world (**Figure 5a**). Visualizing these variants across the Nextstrain derived phylogenetic tree (**Figure 5b**), demonstrated that the highest frequency of these variants (1059C>T, 25563G>T), defined a novel subclade of A2a, which we call A2a-25563. This subclade comprised 82% (281 / 344) of (NYPH-WCMC and GISAID) NYC samples, and 92.7% (281/303) of the A2a portion of NYC cases. Interestingly, while both of the NYPH-WCMC A2a cases harboring the aforementioned NSP1 9-bp deletion were in A2a-25563, many of the remaining cases were distributed across other subclades. Unlike the 6 SNVs used to define A2a-25563, this deletion appeared to be highly polyphyletic with 7 unique phylogenetic clusters associated with the deletion across a variety of clades (**Figure 4c**, **Figure 5b**).

Investigating the geographical and temporal distribution of non-NYC samples in A2a-25563, we found a global distribution with likely origin in Western Europe (Figure 5c, 5d). The first noted case of A2a-25563 in GISAID was in Belgium on 2/21/2020, but since then, this putative subclade has represented a minority (20%) of Western European cases. While the prevalence of

A2a-25563 in NYC appeared to be consistently high across sampling dates, it constituted only a moderate proportion of cases from the Western USA (<50%) in early March with an increase (>78%) in late March (**Figure 5d**). The SNV's defining this subclade were non-synonymous variants targeting genes encoding the non-structural protein 2 (NSP2), the viral replicase, and ORF3a, a poorly characterized SARS-CoV-2 protein with putative roles in inflammation (Siu *et al.*, 2019). This subclade defining ORF3a site (p.Gln57His) was distinct from that which defines the previously characterized L strain (p.Leu84Ser) (Tang *et al.*, 2020).

Defining the SARS-CoV-2 Host Transcriptome

We leveraged the comprehensive nature of the total RNA-seq profiles to define the host transcriptome during SARS-CoV-2 infection. We first integrated the LAMP, qRT-PCR, and total RNA-Seq viral load estimates to identify a final set of 93 SARS-CoV-2 positive (COVID-19 positive) and 204 negative (COVID-19 negative) cases with coverage across the host and viral genomes. Differentially expressed genes (DEGs) associated with SARS-CoV-2 infection were calculated using DESeq2. (see Methods). Overall, 5,982 significant DEGs ($q < 0.01$, >1.5-fold change) were found for the COVID-19 positive samples (**Supp. Table 3**), spanning 2,942 up-regulated DEGs and 3,040 down-regulated DEGs, which could be separated into high, medium, and low viral response categories based on the three detection methodologies (qRT-PCR, NGS, and LAMP) (**Figure 6b**). To test for the possibility of cell proportion changes due to infection, we used Bisque to predict the cell types for all COVID samples, which showed consistent cell distributions of mostly goblet and ciliated airway cells for all samples (**Supp. Figure 9**)

Differentially expressed host genes indicated a wide range of antiviral responses, including some a common interferon response across all ranges of viral levels (**Figure 6b**). The host transcriptome that exhibited the greatest amount of DEGs were those with the highest viral titer. Notably, host epithelial cells showed an increase in angiotensin converting enzyme 2 (*ACE2*) expression (q -value=0.006), which is the SARS-CoV-2 cellular receptor (Hoffmann *et al.*, 2020). This critical gene for viral entry exhibited a dose-dependent expression concomitant with the higher levels of SARS-CoV-2 virus, along with IFI27 (Interferon Alpha Inducible Protein 27) and IFI6 (Interferon Alpha Inducible Protein 6) (**Figure 6c**). Other interferon-related genes included IFIT1, an interferon-induced antiviral RNA-binding protein that specifically binds single-stranded RNA bearing a 5'-triphosphate group (PPP-RNA) and SHFL (Shiftless Antiviral Inhibitor of Ribosomal Frameshifting). The DEGs also included HERC6 (HECT Containing E3 Ubiquitin Protein Ligase Family Member 6), which aids Class I MHC-mediated antigen processing and Interferon-Stimulated Genes (ISG) (**Figure 6c, 6d**), underscoring the impact of the virus on these cells' immune response (Oudshoorn *et al.*, 2012). Also, a subset of cytokines (CXCL10, CXCL11, CCL8) showed the highest spike of expression in the higher viral load subgroup (**Supp. Figure 10**), matching previous results from animal models and infected cells (Blanco-Melo *et al.*, 2020).

Down-regulated genes and those with a negative enrichment score (NES) were functionally distinct (**Figure 6d**). These included *ALAS2*, a gene which makes erythroid ALA-synthase (Ajioka *et al.*, 2006) that is found in developing erythroblasts (red blood cells). ALA-synthase plays an important role in the production of heme TRIM2 E3 ubiquitin ligase induced during late erythropoiesis, which indicated a connection to hematological and iron (heme) regulation during infection (**Figure 6d**). Accordingly, genes in a related biological network were significantly

enriched based on Gene Ontology (GO) pathways for iron regulation (q-value =0.002, **Supp. Table 4**). Both the up-regulated and down-regulated gene expression differences in were distinct from those of house-keeping genes (**Supp. Figure 11**), which stayed mostly stable during infection.

ACEI usage correlates with severe COVID-19 disease

Given our observation of increased *ACE2* gene expression in patients with high SARS-CoV-2 viral load, we broadly investigated the interplay of receiving pharmacologic angiotensin converting enzyme inhibition (ACEI) for hypertension and clinical features of COVID-19 disease. Since *ACE2* expression can be increased in patients taking ACEIs, the observed correlation of viral titer with *ACE2* expression may be attributed to the pre-infection use of such inhibitors, which is common in older patients and those with comorbidities (Fang *et al.*, 2020). To address this, we analyzed an observational cohort of 8,278 patients with suspected SARS-CoV-2 infection from NYPH-CUIMC were analyzed for their usage of ACEIs (4,574 who tested positive). We found that use of ACEIs was strongly associated with testing positive in patients suspected of SARS-CoV-2 infection (Odds Ratio, OR=3.06, and 95% Confidence Interval, CI= 2.38-3.94, $p=2.44E^{-18}$). This result was also consistent when corrected for age, sex, and IL-6, where exposure to ACEIs has an OR=1.54, and when corrected for other reported clinical covariates (1.18-2.01, $p=1.41E^{-03}$); patients exposed to ACEIs were 1.85 (1.40-2.44, $p=1.71E^{-05}$) times more likely to test positive. In the univariate analysis, ACEI usage conferred an increased risk of intubation and mortality for SARS-CoV-2 positive patients (**Table 1**) (intubation: HR=2.63 95%CI: 2.01-3.43, $p=1.22E^{-12}$) (**Figure 6e**) and mortality: HR=1.68 95%CI: 1.22-2.31, $p=1.42E^{-03}$) (**Figure 6f**).

In a multivariate analysis that included age, sex, and IL-6 levels, a significant association between exposure to ACEIs and those requiring mechanical respiration was also found (HR=1.83 95%CI: 1.39-2.40, $p=1.27E^{-05}$). Additionally, this association held when correcting for previously reported risk factors for SARS-CoV-2 morbidity and mortality with an HR=1.56 95%CI: 1.18-2.07, $p=1.83E^{-03}$) (**Supp. Figure 12a**). Moreover, we confirmed previously reported risk factors for both mechanical respiration and mortality. For requirement of mechanical respiration, we found significant effects from male sex ($p=6.18E^{-03}$), diabetes ($p=1.00E^{-03}$), and IL-6 ($p=5.85E^{-113}$). In addition, for mortality we found significant effects from age ($p=8.05E^{-72}$), male sex ($p=6.13E^{-04}$), diabetes ($p=6.66E^{-05}$), and IL-6 ($p=1.26E^{-12}$). Finally, in a post-hoc comparative analysis between specific ACEIs, we found that benazepril was associated with significantly increased risk of mortality (N=32, HR=2.37 95%CI: 1.05-5.35, $p=3.70E^{-02}$) (**Supp. Figure 12b**).

Discussion

These data demonstrate unique host transcriptome profiles during viral infection with SARS-CoV-2, as well as clade-specific mutational landscapes of the virus, both representing the early phase of the U.S. pandemic (March 2020). Total RNA-seq (ribo-depleted RNA) used here enabled a comprehensive molecular map for the virus and host, including complete genotypes (including insertions and deletions) across the length of the viral genome and coding and non-coding RNA gene expression quantification. Moreover, we show that LAMP is a quick (30-minute) and effective assay that could be readily deployed to aid current and future viral testing and surveillance, since it is comparable to RNA-seq and qRT-PCR and can be used with

oropharyngeal swab lysate. Widespread testing is critical to help inform individual quarantine efforts and overall management of highly infectious and long-shedding viruses such as SARS-CoV-2, and these data, methods, and results can help guide future clinical and research efforts.

During a large-scale pandemic with exponential spread, such as COVID-19, scalable methods for diagnosis and screening are crucial for both mitigation and containment (Lan *et al.*, 2020, Liu *et al.*, 2020). While hospital-grade, core lab devices can achieve massive throughput (thousands of samples per day), a key limitation of these assays is accessibility of testing facilities (even roadside testing stations) to patients and the logistics of sample transport and timely test reporting. These limitations become even more stark in the context of widespread quarantines and nationwide lockdowns, where requiring patients to travel (even for viral testing) incurs significant personal and public health risks. The most urgent diagnostic need in this situation is for scalable rapid point-of-care tests that can be potentially implemented in the home. Our validation of a rapid one-tube colorimetric SARS-CoV-2 assay with both qRT-PCR and total RNA-seq provides a potential solution to this problem. Further work will be needed to assess whether this LAMP assay can detect the presence of SARS-CoV-2 at lower (but clinically relevant) viral concentrations in specimen types that are less cumbersome to collect than naso- / oro- pharyngeal swabs (e.g. saliva, stool). As we demonstrate, this LAMP SARS-CoV2 can be also applied for environmental sampling, which may be crucial in the containment phase of this pandemic. Specifically, LAMP positivity may quickly indicate if an area is infectious and a negative result (with appropriate confirmation) will possibly represent a lower risk. Indeed, these tools and methods can help create a viral “weather report” if broadly used and partnered with continual validation.

Total RNA-sequencing data enabled a complete genetic map of the viruses in a significant subset of our samples. Our phylogenetic analysis nominates an A2a subclade (A2a-25563, defined by 25563G>T) which comprises the majority of known NYC samples (including those sequenced outside of this study) (Gonzalez-Reiche *et al.*, 2020). Though remaining NYC cases show a wide distribution across all identified clades, the predominance (>80% in NYC) of such a narrowly defined set of sequences within NYC from a rare ($\leq 20\%$) Western European subclade is striking. These results suggest either (1) a very early introduction by a single patient harboring A2a-25563; or (2) multiple A2a-25563 founder events; or (3) disproportionate community transmission of strains within this subclade. The latter possibility could be consistent with A2a-25563 harboring differential fitness with respect to transmissibility or virulence relative to other A2a viruses. Future studies correlating viral genotypes with patient outcomes in larger cohorts will be necessary to determine whether any of these A2a-25563 associated variants, including the 9 bp in-frame deletion in NSP1 (p.141_143KSD), functionally influence viral transmission or disease severity. The polyphyletic pattern of NSP1 p.141_143KSD, comprising both patients within and beyond A2a-25563, including clades outside of A2a, raises the possibility that this variant arose multiple times and may be under positive selection. Given the small number of these variants observed in our analysis (14), larger and more statistically powered datasets will be required to evaluate this hypothesis.

Although much of the pathophysiology of the novel coronavirus, SARS-CoV-2, remains unknown, studies have reported the virus using the receptor ACE2 for entry into target cells (Hoffman *et al.*, 2020; Lu *et al.*, 2020). Further validating this, we found expression of the *ACE2*

gene was significantly upregulated in the samples with higher viral load, as well as some cytokine genes, which matches observations found in other betacoronaviruses (Sajuthi *et al.*, 2020). ACE inhibitors are commonly used in COVID-19 patients with comorbidities of hypertension, diabetes mellitus, and coronary heart diseases (Fang *et al.*, 2020, Ferrario *et al.*, 2005), indicating to physicians that patients on these medications may be more susceptible to SARS-CoV-2 infection. Indeed, since epidemiological studies have reported increased mortality and morbidity in COVID-19 patients with hypertension, more research needs to be done to address other confounding variables including other comorbidities and treatment with ACE inhibitors or angiotensin receptor blockers (Patel and Verma, 2020).

Although these data alone cannot establish causality between infection and ACE2 expression regulation, they provide some testable hypotheses. For example, if some patients are more susceptible because they are already expressing high levels of ACE2, this could help with targeting ACE2 in these patients as a prophylactic method. However, if the cells respond to infection with ACE2 expression, and this leads to the cytokine storm seen in patients, then this could be used as a downstream treatment (post-infection), for when ACE2 interacts with TMPRSS2, such as the ongoing trials with camostat mesylate (Hoffman *et al.*, 2020). Moreover, SARS-CoV-2 has been found to induce phosphorylation of STAT1 and increases in ISG proteins, a mechanism not previously seen in SARS-CoV, suggesting a potential molecular mechanism behind the upregulation of interferon response (Lokugamage *et al.*, 2020).

Finally, it is notable that the majority of the testing for SARS-CoV-2 so far has relied on nasopharyngeal specimen collection, yet preliminary results here and elsewhere demonstrate that COVID-19 prediction from oral collection could be a more optimal path forward (Woelfel *et al.*, 2020). However, further studies comparing nasopharyngeal, oropharyngeal, and buccal collection approaches, as well as a comparison of different swab types, are needed. Depending on the availability of reagents and resources, as well as automation, a LAMP-based approach on such sample types could allow facilities to increase testing capabilities by orders of magnitude. Since viral pandemics can have significant, long-lasting detrimental impacts for affected countries, it is crucial to deploy methods that can track and profile cases (e.g. RNA-seq, LAMP, qRT-PCR) and provide a comprehensive view of host and viral biology. These methods can help mitigate the medical and socioeconomic harm from viral outbreaks, as well as establish protective surveillance networks that can help defend against future outbreaks.

Acknowledgements

We thank the Core Facilities at Weill Cornell Medicine, the Clinical Laboratories at New York Presbyterian Hospital, the Scientific Computing Unit (SCU), OneCodex, the XSEDE Supercomputing Resources and the GISAID Initiative curators and submitters (**Supp Table 6**). We also thank New England Biolabs for providing the reagents for preliminary testing of the LAMP protocols, as well as Eileen Dimalanta and Ted Davis for technical discussions. The authors wish to thank the following members of the HudsonAlpha Discovery team who supported the RNASeq experiments described in the manuscript: Colleen Cowan, John Mote, Arianna Pionzio, Melanie Robinson, and Madison Robison.

Funding

We are grateful for support from the STARR Foundation (I13-0052) the Vallee Foundation, the WorldQuant Foundation, The Pershing Square Sohn Cancer Research Alliance, Citadel, the National Institutes of Health (R01MH117406, R25EB020393, R01AI151059), the Bill and Melinda Gates Foundation (OPP1151054), the NSF (1840275), the National Center for Advancing Translational Sciences of the National Institutes of Health (UL1TR000457, CTSC), and the Alfred P. Sloan Foundation (G-2015-13964). FJS supported by the National Institute of Allergy and Infectious Diseases (1U19AI144297-01). MZ supported by T15LM007079. NPT and UOG supported by R35GM131905. NAI was supported by the National Center for Advancing Translational Sciences of the National Institutes of Health under Award Number TL1TR002386.

Author Contributions

CEM led the study design and coordination and HR led the clinical collection and validation work in the NYP CLIA laboratory, as well as with MI. Overall supervision and protocol development and implementation for the Zymo RNAClean and NEB assays (SL). DB and CMz performed the LAMP experiments to validate the assay, established a method to quantify LAMP output, and developed a protocol for clinical use of the assay. CeM, DD, JF, AS, JR, MM, EA, IH, DM, MI, BWL, MZ, UG, NiT, NAI, CEM performed analyses. DD, CMz, NAI, MS, BY, KR, CB coordinated and collected environmental samples. EA submitted the IRB application and helped with clinical coordination. Help and insights for analysis from EA, SL, MI, MS, LFW, ML, MC, HR, KR all led to the figures and analyses. All authors reviewed, edited, and approved the manuscript.

Conflicts of Interest

Nathan Tanner and Bradley W. Langhorst are employees at New England Biolabs.

IRB

Samples were collected and processed through the Weill Cornell Medicine Institutional Review Board (IRB) Protocol 19-11021069. Observational cohort analysis (ACEI) was done through the Columbia University IRB Protocol AAAL0601.

Data Accessibility

Viral sequences were uploaded into GISAID (Global Initiative on Sharing All Influenza Data) site (<https://www.gisaid.org>), and patient data is deposited into dbGAP.

Materials and Methods

Sample Collection and Processing

Patient specimens were collected with patients' consent at New York Presbyterian Hospital-Weill Cornell Medical Center (NYPH-WCMC) and then processed for qRT-PCR.

Nasopharyngeal (NP) swab specimens were collected using the BD Universal Viral Transport Media system (Becton, Dickinson and Company, Franklin Lakes, NJ) from symptomatic patients.

Extraction of Viral RNA and qRT-PCR detection

Total viral RNA was extracted from deactivated samples using automated nucleic acid extraction on the QIAAsymphony and the DSP Virus/Pathogen Mini Kit (QIAGEN). One step reverse transcription to cDNA and real-time PCR (RT-PCR) amplification of viral targets, E (envelope) and S (spike) genes and internal control, was performed using the Rotor-Gene Q thermocycler (QIAGEN).

Twist Synthetic RNAs

We used two fully synthetic RNAs made by in vitro transcription (IVT) from Twist Biosciences, which were synthesized in 5kb pieces with full viral genome coverage of SARS-CoV-2. They were sequence verified to ensure >99.9% viral genome coverage, and come as 1,000,000 copies per μL , 100 μL per tube. The two controls are from Wuhan, China (MN908947.3) and Melbourne, Australia (MT007544.1). Reference sequence designs came from NCBI: <https://www.ncbi.nlm.nih.gov/nuccore/MT007544> and <https://www.ncbi.nlm.nih.gov/nuccore/MN908947.3>.

Reverse Transcriptase, quantitative real-time PCR (RT-PCR)

Clinical samples were extracted as described above and then tested with qRT-PCR using primers for the E (envelope) gene, which detects all members of the lineage B of the beta-CoVs, including all SARS, SARS-like, and SARS-related viruses, and a second primer set for the S (spike) gene, which specifically detects the SARS-CoV-2 virus. The reaction also contains an internal control that served as an extraction control and a control for PCR inhibition.

Samples were annotated using qRT-PCR cycle threshold (Ct) value for SARS-CoV-2 primers. Subjects with Ct less than or equal to 18 were assigned "high viral load" label, Ct between 18 and 24 were assigned "medium viral load" and Ct between 24 and 40 were assigned "low viral load" classes, with anything above Ct of 40 was classified as negative. We also predicted a combined viral load score using Ct, GloMax QuantiFluor readout from LAMP experiments and fraction of SARS-CoV-2 matching NGS reads in a sample. For this score (40-Ct), (LAMP readout) and ($\log_{10}(\text{SARS-CoV-2 fraction} + 1e-6)$) were all normalized between zero and one individually, and summed together using a combination weight of 5 for Ct, 3 for LAMP and 2 for NGS.

LAMP Primer Sequences

Primers were designed using PrimerExplorer (v4.0), as per guidelines in Zhang *et al.*, 2020. This specifically utilized the LAMP-compatible primers for the on the COVID-19 reference genome (NCBI). LAMP's inherent specificity (using 4-6 primers vs. 2 for PCR amplification) in combination with this *in-silico* analysis revealed there is limited opportunity for cross-reactivity to allow for false-positive reporting or affect performance of the N-gene primers for SARS-CoV-2 detection (**Supp Table 5**). Overall, the primers had less than 80% homology with the vast majority of tested pathogen sequences. For any organisms where a primer hit >80% homology, only one of the primers (forward or reverse) had significant homology making an amplified product extremely unlikely. Overall, the results of this analysis predict no significant cross-reactivity or microbial interference. We also assessed the potential impact of sequence variation in circulating strains that might lead to poor amplification. In the thousands of sequences deposited in GISAID (Shu and McCauley, 2017), only one site in the priming region was observed to be polymorphic. The polymorphism (T30359C) was only observed in 106 of 6753

(<2%) sequences with coverage of this region. This variant overlaps the priming site of the LB primer but is not near a 3-prime end and is not anticipated to cause amplification failure.

Nucleocapsid Gene: (N, 5'-3'):

GeneN-F3 TGGCTACTACCGAAGAGCT

GeneN-B3 TGCAGCATTGTTAGCAGGAT

GeneN-FIP TCTGGCCCAGTTCCTAGGTAGTCCAGACGAATTCGTGGTGG

GeneN-BIP AGACGGCATCATATGGGTTGCACGGGTGCCAATGTGATCT

GeneN-LF GGA CTGAGATCTTTCATTTTACCGT

GeneN-LB ACTGAGGGAGCCTTGAATACA

Primer Sequences: rActin (5'-3')

ACTB-F3 AGTACCCCATCGAGCACG

ACTB-B3 AGCCTGGATAGCAACGTACA

ACTB-FIP GAGCCACACGCAGCTCATTGTATCACCAACTGGGACGACA

ACTB-BIP CTGAACCCCAAGGCCAACCGGCTGGGGTGTGAAGGTC

ACTB-LoopF TGTGGTGCCAGATTTTCTCCA

ACTB-LoopB CGAGAAGATGACCCAGATCATGT

The LAMP Reaction Setup

For each well or Eppendorf tube, we utilized a set of six primers (above) for Gene N, the M1800 LAMP Master Mix (NEB), water, and 11.5µL of the sample. The protocol is as follows:

1. Reagents added:
 - a. 12.5 µL M1800 LAMP mix (NEB)
 - b. 1 µL LAMP primers (Gene N)
 - c. 1-11.5 µL of sample
 - d. Remaining volume (to 25 µl) H₂O
2. Vortex, spin down;
3. Place on Thermocycler at 65°C for 30 minutes with lid at 105 °C;
4. Remove tubes, place on ice for 5 seconds;
5. Visualize over lab bench/ice/paper.

Light Intensity and Data Processing

Completed reactions were analyzed with the Promega GloMax Explorer (Promega GM3500) fluorometer using the QuantiFluor ONE dsDNA system (Promega E4871). This system recorded light intensity from each well using an emission filter of 500-550nm, an excitation filter set at blue 475 nm, and a high sensitivity setting on the Glomax software. Values were then tabulated and compared with controls (positive and negative). The intensity threshold of 2.5x negative control was used as the threshold for positive detection.

DNase treatment, rRNA depletion, and RNAseq library construction

All samples' total nucleic acid (TNA) were treated with DNase 1 (Zymo Research, Catalog # E1010), which cuts both double-stranded and single-stranded DNA. Post-DNase digested samples were then put into the NEBNext rRNA depletion v2 (Human/Mouse/Rat), Ultra II Directional RNA (10ng), and Unique Dual Index Primer Pairs were used following the vendor

protocols from New England Biolabs (except for the first flowcell, see supplemental figures). Kits were supplied from a single manufacturer lot. Completed libraries were quantified by Qubit or equivalent and run on a Bioanalyzer or equivalent for size determination. Libraries were pooled and sent to the WCM Genomics Core, HudsonAlpha, or New York Genome Center for final quantification by Qubit fluorometer (ThermoFisher Scientific), TapeStation 2200 (Agilent), and QRT-PCR using the Kapa Biosystems Illumina library quantification kit.

Taxonomic Classification of Sequence Data

All complete genome or chromosome level assemblies from RefSeq database for archaea, bacteria, protozoa, fungi, human and viruses including SARS-CoV and SARS-CoV-2 genomes were downloaded and used for building a classification database for Kraken2 ($k=35$, $\ell=31$) (O'Leary *et al.*, 2016; Wood *et al.*, 2019).

To get an approximation for the positive and negative classification rate, the BBMap random-reads script was used to simulate 10 million 150bp paired-end Illumina reads from the database sequences (Segata *et al.*, 2016). For the negative test all sequences in the database excluding SARS-CoV and SARS-CoV-2 genome were removed from the sequences and the simulated reads were mapped with the Kraken2 database (Supp Table 1).

For the positive test, the same process was repeated using only SARS-CoV-2 genome (**Supp Table 1**). Positive results show >99% of SARS-CoV-2 reads uniquely map to either SARS-CoV or SARS-CoV-2, with the remaining 1% are ambiguous, potentially matching multiple taxa (**Supp Table 2**). All sequences were classified using the Kraken2 database. To remove the potential contamination of reads that are homologous across multiple species we used Kraken2 outputs to filter sequences to either human (uniquely matching *Homo sapiens* and no other taxon in our database), SARS-CoV-2 (either matching SARS-CoV or SARS-CoV-2 due to homology between these two viruses), and remaining reads that may be coming from unclassified, archaeal, bacterial, viral, fungal, protozoan or ambiguously mapping reads to human or SARS-CoV (Li, 2015).

Reference- and Fragment-based Viral Mapping and Assembly

Reads unambiguously mapping to SARS-CoV or SARS-CoV-2 were aligned to the Wuhan-Hu-1 (Genbank accession MN908947.3) reference using *bwa mem* (Li, 2013). Variants were called using *iVar*, and pileups and consensus sequences were generated using *samtools* (Li *et al.*, 2009; Grubaugh *et al.*, 2019; Greenfield *et al.*, 2020). Any sample with more than 30,000 SARS-CoV-2 mapping reads and >99% coverage above 10x depth were taken as reliable samples, which resulted in 95 samples (90 positive, 2 negative, 2 positive controls and 1 negative control). 92 clinical samples were compared to 4872 SARS-CoV-2 sequences from GISAID (as of April 10, 2020) (9, 10). All sequence filtering, alignments, phylogenetic inference, temporal ordering of sequences and geographic reconstruction of likely transmission events were done using *nextstrain* (Kato and Standley, 2013; Sagulenko *et al.*, 2018; Hadfield *et al.*, 2018).

Fragment assembly was also performed using IRMA (Sehpard *et al.*, 2016). The Wuhan-Hu-1 genome (Genbank accession MN908047.3) was used as a reference with the poly-A tail trimmed to reduce the likelihood of false low-complexity matching. An HMM model of this reference sequence was created using the *native modelfromalign* script. IRMA was run with the COV

module with the following parameters adjusted from the default: minimum read length = 25bp; minimum read pattern count = 5; minimum read count = 2; minimum count for alternative finished assembly = 20. Consensus assemblies were aligned to the Wuhan-Hu-1 reference using MAFFT (Katoh and Standley, 2013) with default settings, and sequence identity and coverage metrics were calculated using Mview (Brown *et al.*, 1998). Phylogenetic trees were created using nextstrain's augur as described above, and visualized using the ggtree package in R (Yu, 2020).

Viral SNV Calling

Subsequent to alignment, SNV were identified by xAtlas (Farek *et al.*, 2018) (parameters: -g -m 10 -n 10) producing a gVCF per sample. The individual call sets were merged using bcftools (Li, 2011) (merge -g) and allele counts were added with bcftools view (-q 0.01). Population-level variants across all samples were converted in a presence/absence matrix using a customized script where every SNV was counted as present if it was supported by at least 5% of the reads. This matrix was loaded in R and underwent hierarchical clustering using the function dist with the euclidean method and hclust using the average method. All samples were further analyzed using Manta (Chen *et al.*, 2016), and subsequently summarized and filtered using the SURVIVOR pipeline (Jeffares *et al.*, 2017). Subsequently, SV calls were re-genotyped using SVTyper (doi:10.1038/nmeth.3505) and a population-level VCF was generated using SURIVOR merge (allowing for 100bp maximum distance). Events were filtered for only <1000bp insertions and deletions that were homozygous in a sample.

Human Transcriptome Analysis

The reads that mapped unambiguously to the human reference genome via Kraken2 were used to detect the host transcriptional response to the virus. Reads matching *Homo sapiens* were trimmed with TrimGalore, aligned with STAR (v2.6.1d) to the human reference build GRCh38 and the GENCODE v33 transcriptome reference, gene expression was quantified using featureCounts, stringTie and salmon using the nf-core RNAseq pipeline (Pertea *et al.*, 2015; Malinen *et al.*, 2005; Johnson *et al.*, 2007; Robinson *et al.*, 2010; Naccache *et al.*, 2014; Zamani *et al.*, 2017; Ewels *et al.*, 2019). Sample QC was reported using fastqc, RSeQC, qualimap, dupradar, Preseq and MultiQC (Okonechnikov *et al.*, 2016; Andrews, 2015; Ewels *et al.*, 2016; Sayols *et al.*, 2016; Wang *et al.*, 2012). Samples that had more than 10 million human mapped reads were used for differential expression analysis. Reads, as reported by featureCounts, were normalized using variance-stabilizing transform (vst) in DESeq2 package in R (Love *et al.*, 2014) for visualization purposes in log-scale. DESeq2 was used to call differential expression with either Positive cases vs Negative, or viral load (High/Medium/Low/None) as reported by either qRT-PCR cycle threshold (Ct) values or the combination viral load method as explained before. Genes with BH-adjusted p-value < 0.01 and absolute log₂ fold-change greater than 0.58 (at least 50% change in either direction) were taken as significantly differentially regulated (Benjamini and Hochberg, 1995). The complete gene list for all comparisons are given in Supp Table 3. Resulting gene sets were ranked using log₂ fold-change values within each comparison and put into GSEA to calculate gene set enrichment for molecular signatures database (MSigDB), MGI Mammalian Phenotypes database and ENCODE transcription factor binding sets (Liberzon *et al.*, 2011; Subramanian *et al.*, 2005; Sergushichev, 2016; Smith *et al.*, 2018). Any signature with adjusted p-value < 0.01 and absolute normalized enrichment score (NES) >= 1.5 were reported (Supp Table 3).

Cell Deconvolution Analysis

Bulk RNAseq count data was deconvoluted into cell composition matrices using the Bisque algorithm (<https://www.biorxiv.org/content/10.1101/669911v1.full>) on a reference single cell RNAseq data from upper respiratory epithelium obtained from nasal brushes (<https://www.nature.com/articles/s41591-019-0468-5>).

Cross-reactivity Analysis

Primers were compared with a list of sequences from organism from the same genetic family as SARS-CoV-2 and other high-priority organisms listed in the United States Food and Drug Administration's Emergency Use Authorization Template (<https://www.fda.gov/media/135900/download>). Using the sequence names in the EUA template, the NCBI taxonomy database was queried to find the highest quality representative sequences for more detailed analysis. Primers were compared to this database using Blast 2.8.1 and the following parameters (word size: 7, match score: 2, mismatch score: -3, gap open cost: 5, gap extend cost: 2). Up to 1000 hits with e-value > 10 were reported.

Inclusivity Analysis

Unique, full-length, human-sample sequences were downloaded from the GISAID web interface. These sequences were aligned to NC_045512.2 (Wuhan SARS-CoV-2) using minimap2 -x asm5 and visually inspected using IGV 2.8.0 with allele frequency threshold set to 0.01.

ACE Inhibitor Cohort Analysis

We compared usage of ACE inhibitors in an observational cohort analysis of 8,278 patients with suspected SARS-CoV-2 infection (4,574 of which tested positive). ACE inhibitors are commonly taken continuously for several years (Bonarjee et al., 2001). We defined a cohort of ACE inhibitor-exposed patients as those that have an ACE inhibitor prescription order sometime after January 1st, 2019. We compared the frequency of ACE inhibitor exposure in three cohort comparisons:

- i. SARS-CoV-2 tested positive patients versus SARS-CoV-2 tested negative patients,
- ii. SARS-CoV-2 positive patients who require mechanical ventilation versus those who did not, and
- iii. SARS-CoV-2 positive patient survival versus death.

In addition, we perform one post-hoc comparison to evaluate the individual effects of particular ACE inhibitors among SARS-CoV-2 positive patients who are exposed to ACE inhibitors.

Cohort and Data Source

Our cohort data for SARS-CoV-2 suspected patients is extracted from the electronic health records at New York-Presbyterian Hospital-Columbia University Irving Medical Center (NYPH-CUIMC). We used data collected starting on March 10th, 2020 through April 16th, 2020. In addition, we used data from 279,487 patients, who were not tested for SARS-CoV-2 infection, with available electronic health records from January 1st, 2019 through September 24th, 2019 to represent a comparison population of patients. In both cases, data extracted included disease diagnoses, laboratory measurements, medication and pharmacy orders, and patient demographics. We derived mortality from a death note filed by a resident or primary provider that records the date and time of death. Intubation was used as an intermediary endpoint and is a

proxy for a patient requiring mechanical respiration. We used note types that were developed for patients with SARS-CoV-2 infection to record that this procedure was completed. We validated outcome data derived from notes against the patient's medical record using manual review.

Experimental Statistical Methods

We conducted univariate analysis of the frequency differences of ACE inhibitor exposure and multivariate regression analysis to account for established risk factors for SARS-CoV-2 outcomes (i.e. age, sex, and baseline IL-6 upon admission (Zhou et al., 2020)). We use logistic regression for analysis for comparing cohort (i) as this cohort is retrospective analysis on patients with definitive outcomes. We perform survival analysis using a Cox proportional hazards model for cohort comparisons (ii) and (iii) as some patients from these cohorts are currently being treated and their outcomes are unknown (i.e., censored). We cannot determine from our data the date of infection. For the study start date for the patient, we use the date of testing positive minus seven days. Quantitative variables (i.e., age and the first IL-6 measurement) are scaled to [0,1] to facilitate comparison of model coefficients to those of dichotomous variables. Prior to conducting our multivariate analysis, we evaluated and removed correlated covariates. We include a model built with all covariates as well in the supplemental tables.

Comorbidity Definitions

Risk factors were assigned using OMOP CDM concept IDs 317576 for “Coronary Arteriosclerosis”, 201820 for “Diabetes mellitus”, and 437525 for “Overweight”. In each case, the concept ID and all descendant concepts were used to define the risk factor phenotype, and individuals were assigned the phenotype if they were assigned any of the codes.

Statistical and visualization Software

All analyses were done in using Python 3.7 and all models were fit using R 3.6.3. Survival analyses (Cox regressions and survival curves) were performed with the survival package for R, version 3.1-12. Statistics and visualization of single nucleotide variants and indels were completed in R. Visualization of phylogenies was completed using Auspice and the ‘ape’ library for R.

References

Ajioka RS, Phillips JD, Kushner JP. Biosynthesis of heme in mammals. *Biochim Biophys Acta*. 2006 Jul;1763(7):723-36

Amanat F, Nguyen T, Chromikova V, Strohmeier S, Stadlbauer D, Javier A, Jiang K, Asthagiri-Arunkumar G, Polanco J, Bermudez-Gonzalez M, Caplivski D, Cheng A, Kedzierska K, Vapalahti O, Hepojoki J, Simon V, Krammer F. A serological assay to detect SARS-CoV-2 seroconversion in humans. *MedRxiv*. 2020 Mar 18.

<https://www.medrxiv.org/content/10.1101/2020.03.17.20037713v1>

Andrews S. FASTQC A Quality Control tool for High Throughput Sequence Data. *Babraham Inst.* (2015).

Benjamini Y, Hochberg Y. Controlling the False Discovery Rate: A Practical and Powerful Approach to Multiple Testing. *J. R. Stat. Soc. Ser. B* (1995)

Broughton JP, Deng X, Yu G, Fasching CL, Singh J, Streithorst J, Granados A, Sotomayor-Gonzalez A, Zorn K, Gopez A, Hsu E, Gu W, Miller S, Pan C, Guevara H, Wadford D, Chen J, Chiu CY. Rapid Detection of 2019 Novel Coronavirus SARS-CoV-2 Using a CRISPR-based DETECTR Lateral Flow Assay. 2020 Mar; 10: 1-27.

<https://medrxiv.org/cgi/content/short/2020.03.06.20032334v1>

Brown, N.P., Leroy C., Sander C. (1998). MView: A Web compatible database search or multiple alignment viewer. *Bioinformatics*. 14 (4):380-381.

Chen X, Schulz-Trieglaff O, Shaw R, Barnes B, Schlesinger F, Källberg M, Cox AJ, Kruglyak S, Saunders CT. Manta: rapid detection of structural variants and indels for germline and cancer sequencing applications, *Bioinformatics*, Volume 32, Issue 8, 15 April 2016, Pages 1220–1222

Chiang C, Layer RM, Faust GG, Lindberg MR, Rose DB, Garrison EP, Marth GT, Quinlan AR, Hall IM. SpeedSeq: Ultra-fast personal genome analysis and interpretation. *Nature Methods* 12(2015): 966–968.

Danko D, Bezdán D, Afshinnekoo E, et al...Mason CE. Global Genetic Cartography of Urban Metagenomes and Anti-Microbial Resistance

<https://www.biorxiv.org/content/10.1101/724526v1>

Deng X, Achari A, Federman S, Yu G, Somasekar S, et al...Chiu CY. Metagenomic sequencing with spiked primer enrichment for viral diagnostics and genomic surveillance. *Nature Microbiology*. 2020 Mar; 5(3): 443–454.

Dong E, Du H, Gardner L. An interactive web-based dashboard to track COVID-19 in real time. *Lancet Infect Dis*. 2020 Feb 4.

Elbe S, Buckland-Merrett G. Data, disease and diplomacy: GISAID's innovative contribution to global health. *Glob. Challenges* (2017)

Ewels P, Magnusson M, Lundin S, Käller M. MultiQC: Summarize analysis results for multiple tools and samples in a single report. *Bioinformatics* (2016)

Ewels PA et al., nf-core: Community curated bioinformatics pipelines. *Nature* 2020 Feb 13.

Farek J, Hughes D, Mansfield A, Krasheninina O, Nasser W, Sedlazeck FJ, Khan Z, Venner E, Metcalf G, Boerwinkle E, Muzny DM, Gibbs RA, Salerno W. xAtlas: Scalable small variant calling across heterogeneous next-generation sequencing experiments. bioRxiv 295071; doi: <https://doi.org/10.1101/295071>

Fang L, Karakiulakis G, Roth M. Are patients with hypertension and diabetes mellitus at increased risk for COVID-19 infection? *Lancet Respir Med*. 2020 Apr;8(4):e21.

Fauver JR, et al., Coast-to-coast spread of SARS-CoV-2 during the early epidemic in the United States. *Cell* 2020.

Gardy J, Loman NJ, Rambaut A. Real-time digital pathogen surveillance - the time is now. *Genome Biology*. 2015 Jul 30;16(1):155.

Gonzalez-Reiche A, Hernandez MH, Sullivan M, Ciferri B, Alshammary H, Obla A, Fabre S, Kleiner G, Polanco J, Khan Z, Albuquerque B, Guchte A, Dutta J, Francoeur N, Salom B, Oussenko I, Deikus G, Soto J, Sridhar SH, Wang Y, Twyman K, Kasarskis A, Altman DR, Smith M, Sebra R, Aberg J, Krammer F, Garcia-Sarstre A, Luksza M, Patel G, Paniz-Mondolfi A, Gitman M, Sordillo EM, Simon V, Bakel H. Introductions and early spread of SARS-CoV-2 in the New York City area. *MedRxiv*. 2020. Apr 11.

<https://www.medrxiv.org/content/10.1101/2020.04.08.20056929v1>

Guan WJ, Ni Zy, Hu Y, Liang WH, Ou CQ, He JX, Liu L, Shan H, Lei CL, Hui DSC, Du B, Li LJ, Zeng G, Yuen KY, Chen RC, Tang CL, Wang T, Chen PY, Xiang J, Li SY, Wang JL, Liang ZJ, Peng YX, Wei L, Liu Y, Hu YH, Peng P, Wang JM, Liu JY, Chen Z, Li G, Zheng ZJ, Qiu SQ, Luo J, Ye CJ, Zhu SY, Zhong NS, China Medical Treatment Expert Group for Covid-19. Clinical Characteristics of Coronavirus Disease 2019 in China. *NEJM*. 2020 Feb 28.

Greenfield N, SARS-CoV-2 variant calling and consensus assembly pipeline. GitHub (2020), (available at <https://github.com/onecodex/sars-cov-2/>).

Grubaugh ND et al., An amplicon-based sequencing framework for accurately measuring intrahost virus diversity using PrimalSeq and iVar. *Genome Biol*. (2019)

Hadfield J, Megill C, Bell S, Huddleston J, Potter B, Callender C, Sagulenko P, Bedford T, and Neher RA. 2018. Nextstrain: Real-Time Tracking of Pathogen Evolution. *Bioinformatics* 34 (23): 4121–23.

He F, Deng Y, Li W. Coronavirus Disease 2019 (COVID-19): What we know? *J Med Virol*. 2020 Mar 14.

Hoffmann M, Weber HK, Schroeder Krüger N, Herrler T, Erichsen S, Schiergens TS, Herrler G, Wu N, Nitsche A, Müller MA, Drosten C, Pöhlmann S. SARS-CoV-2 Cell Entry Depends on ACE2 and TMPRSS2 and Is Blocked by a Clinically Proven Protease Inhibitor. *Cell*. 2020. Mar 5.

Jeffares DC, Jolly C, Hoti M, et al. Transient structural variations have strong effects on quantitative traits and reproductive isolation in fission yeast. *Nature Communications*. 2017 Jan;8:14061.

Jenkins C and Orsburn B. In silico approach to accelerate the development of mass spectrometry-based proteomics methods for detection of viral proteins: Application to COVID-19. 2020 Mar 10. <https://www.biorxiv.org/content/10.1101/2020.03.08.980383v1>

Johnson WE, Li C, Rabinovic A. Adjusting batch effects in microarray expression data using empirical Bayes methods. *Biostatistics* (2007).

Konrad R, Eberle U, Dangel A, Treis B, Berger A, Bengs K, Fingerle V, Liebl B, Ackermann N, Sing A. Rapid Establishment of Laboratory Diagnostics for the Novel Coronavirus SARS-CoV-2 in Bavaria, Germany, February 2020. *Eurosurveillance*. 2020 Mar 5.

Kim D, Lee J, Yang J, Kim JW, Kim N, Chang H. The architecture of SARS-CoV-2 transcriptome. *BioRxiv* <https://www.biorxiv.org/content/10.1101/2020.03.12.988865v2>

Lan L, Xu D, Ye G, Xia C, Wang S, Li Y, Xu H. Positive RT-PCR Test Results in Patients Recovered from COVID-19. *JAMA* 2020 Feb 27.

Langmead B, and Salzberg S. 2012. Fast Gapped-Read Alignment with Bowtie 2. *Nature Methods* 9 (4): 357–59.

Lauer SA, Grantz KH, Bi Q, Jones FK, Zheng Q, Meredith HR, Azman AS, Reich NG, Lessler J. The Incubation Period of Coronavirus Disease 2019 (COVID-19) From Publicly Reported Confirmed Cases: Estimation and Application. *Annals of Internal Medicine*. 2020 Mar 10. M20-0504.

Layer RM, Chiang C, Quinlan AR, Hall IM. LUMPY: a probabilistic framework for structural variant discovery. *Genome Biol*. 2014;15(6):R84.

Li H. A statistical framework for SNP calling, mutation discovery, association mapping and population genetical parameter estimation from sequencing data. *Bioinformatics*. 2011;27(21):2987–2993.

Li H, Seqtk: Toolkit for processing sequences in FASTA/Q formats. GitHub (2015).

Li H, Aligning sequence reads, clone sequences and assembly contigs with BWA-MEM. arXiv Prepr. arXiv (2013), doi:arXiv:1303.3997 [q-bio.GN].

Li H et al., The Sequence Alignment/Map format and SAMtools. *Bioinformatics* (2009).

Li R, Pei S, Chen B, Song Y, Zhang T, Yang W, Shaman J. Substantial undocumented infection facilitates the rapid dissemination of novel coronavirus (SARS-CoV2). *Science*. 2020 Mar 16.

Liberzon A et al., Molecular signatures database (MSigDB) 3.0. *Bioinformatics* (2011).

Liu R, Han H, Liu F, Lv Z, Wu K, Liu Y, Feng Y, Zhu C. Positive Rate of RT-PCR Detection of SARS-COV-2 Infection of 4880 Cases from One Hospital in Wuhan, China, from Jan to Feb 2020. *Clinica Chimica Acta* 505 (2020) 172-175.

Lokugamag KG, Hage A, Schindewolf C, Rajsbaum R, Menachery VD. SARS-CoV-2 is sensitive to type 1 interferon pretreatment. *BioRxiv*
<https://www.biorxiv.org/content/10.1101/2020.03.07.982264v3>

Love MI et al., Moderated estimation of fold change and dispersion for RNA-seq data with DESeq2. *Genome Biol.* (2014), doi:10.1186/s13059-014-0550-8.

Lu J et al., Genomic epidemiology of SARS-CoV-2 in Guangdong Province, China. *Cell* 2020

Malinen E et al., Analysis of the fecal microbiota of irritable bowel syndrome patients and healthy controls with real-time PCR. *Am. J. Gastroenterol.* 100, 373–382 (2005).

Metsky HC, Freije CA, Kosoko-Thoroddsen TF, Sabeti PC, Myhrvold C. CRISPR-based surveillance for COVID-19 using genomically-comprehensive machine learning design. 2020 Mar 2. *BioRxiv*. <https://www.biorxiv.org/content/10.1101/2020.02.26.967026v2>.

Meyers L, Dien Bard J, Galvin B, Nawrocki J, Niesters HGM, Stellrecht KA, St George K, Daly JA, Blaschke AJ, Robinson C, Wang H, Cook CV, Hassan F, Dominguez SR, Pretty K, Naccache S, Olin KE, Althouse BM, Jones JD, Ginocchio CC, Poritz MA, Leber A, Selvarangan R. Enterovirus D68 Outbreak Detection Through A Syndromic Disease Epidemiology Network. *J Clin Virol*, 124, 104262, 2020 Mar.

Naccache SN et al., A cloud-compatible bioinformatics pipeline for ultrarapid pathogen identification from next-generation sequencing of clinical samples. *Genome Res.* (2014),

Narayanan K, Ramirez SI, Lokugamage KG, Makino S. Coronavirus nonstructural protein 1: Common and distinct functions in the regulation of host and viral gene expression. *Virus Res.* 2015 Apr 16;202:89-100.

Okonechnikov K, Conesa A, García-Alcalde F. Qualimap 2: Advanced multi-sample quality control for high-throughput sequencing data. *Bioinformatics* (2016),

Ong SWX, Tan YK, Chia PY, Lee TH, Ng OT, Wong MSY, Marimuthu K. Air, Surface Environmental, and Personal Protective Equipment Contamination by Severe Acute Respiratory Syndrome Coronavirus 2 (SARS-CoV-2) From a Symptomatic Patient. *JAMA.* 2020 Mar 4.

O’Leary NA et al., Reference sequence (RefSeq) database at NCBI: Current status, taxonomic expansion, and functional annotation. *Nucleic Acids Res.* (2016).

Oudshoorn D, van Boheemen S, Sánchez-Aparicio MT, Rajsbaum R, García-Sastre A, Versteeg GA. HERC6 is the main E3 ligase for global ISG15 conjugation in mouse cells. *PLoS One.* 2012;7(1):e29870.

Patel AB, Verma A. COVID-19 and Angiotensin-Converting Enzyme Inhibitors and Angiotensin Receptor Blockers. What is the evidence? *JAMA* 2020 Mar 24.

Peci A, Winter AL, King EC, Blair J, Gubbay JB. Performance of rapid influenza diagnostic testing in outbreak settings. *J Clin Microbiol.* 2014 Dec;52(12):4309-17.

Pertea M et al., StringTie enables improved reconstruction of a transcriptome from RNA-seq reads. *Nat. Biotechnol.* (2015)

Quilty B, Clifford S, Flasche S, Eggo RM. Effectiveness of airport screening at detecting travellers infected with 2019-nCoV. 2020. Feb 02. *MedRxiv.*
<https://www.medrxiv.org/content/10.1101/2020.01.31.20019265v1>

Robinson MD, Oshlack A, A scaling normalization method for differential expression analysis of RNA-seq data. *Genome Biol.* (2010).

Rausch T, Zichner T, Schlattl A, Stütz AM, Benes V, Korbel JO. DELLY: structural variant discovery by integrated paired-end and split-read analysis. *Bioinformatics*, Volume 28, Issue 18, 15 September 2012, Pages i333–i339.

Robinson, James T., Helga Thorvaldsdóttir, Wendy Winckler, Mitchell Guttman, Eric S. Lander, Gad Getz, and Jill P. Mesirov. 2011. Integrative Genomics Viewer. *Nature Biotechnology* 29 (1): 24–26.

Santarpia JL, Rivera DN, Herrera V, Morwitzer MJ, Creager H, Santarpia GW, Crown KK, Brett-Major DM, Schnaubelt E, Broadhurst MJ, Lawler JV, Reid SP, Lowe JJ. Transmission Potential of SARS-CoV-2 in Viral Shedding Observed at the University of Nebraska Medical Center. 2020. Mar 26. *MedRxiv.*
<https://www.medrxiv.org/content/10.1101/2020.03.23.20039446v2>

Segata N et al., BBMap short-read aligner, and other bioinformatics tools. *Bioinformatics* (2016).

Sajuthi SP, DeFord P, Jackson ND, Montgomery MT, Everman JL, Rios CL, Pruesse E, Nolin JD, Plender EG, Wechsler ME, Mak A, Eng C, Salazar S, Medina V, Wohlford EM, Huntsman S, Nickerson D, Germer S, Zody MC, Abecasis G, Kang H, Rice KM, Kumar R, Oh S,

Shu Y, McCauley J. GISAID: Global initiative on sharing all influenza data – from vision to reality. *Eurosurveillance* (2017).

Siu KL, Yuen KS, Castaño-Rodríguez C, Ye ZW, Yeung ML, Fung SY, Yuan S, Chan CP, Yuen KY, Enjuanes L, Jin DY. Severe acute respiratory syndrome coronavirus ORF3a protein activates the NLRP3 inflammasome by promoting TRAF3-dependent ubiquitination of ASC. *The FASEB Journal* (2019), doi: 10.1096/fj.201802418R.

Katoh K, Standley DM. MAFFT multiple sequence alignment software version 7: Improvements in performance and usability. *Mol. Biol. Evol.* (2013).

Rodriguez-Santana J, Burchard EG, Seibold MA. Type 2 and interferon inflammation strongly regulate SARS-CoV-2 related gene expression in the airway epithelium. *Biorxiv.* 2020. Apr 10. <https://www.biorxiv.org/content/10.1101/2020.04.09.034454v1>

Sagulenko P, Puller V, Neher RA, TreeTime: Maximum-likelihood phylodynamic analysis. *Virus Evol.* (2018), doi:10.1093/ve/vex042.

Sayols S, Scherzinger D, Klein H. dupRadar: A Bioconductor package for the assessment of PCR artifacts in RNA-Seq data. *BMC Bioinformatics* (2016), doi:10.1186/s12859-016-1276-2.

Sergushichev A, An algorithm for fast preranked gene set enrichment analysis using cumulative statistic calculation. *bioRxiv* (2016), doi:10.1101/060012.

Shepard, S.S., Meno, S., Bahl, J. et al. Viral deep sequencing needs an adaptive approach: IRMA, the iterative refinement meta-assembler. *BMC Genomics* 17, 708 (2016).

Schmid-Burgk JL Li D, Feldman D, Ślabicki M, Borrajo J, Strecker J, Cleary B, Regev A, Zhang F. LAMP-Seq: Population-Scale COVID-19 Diagnostics Using a Compressed Barcode Space. *BioRxiv.* <https://www.biorxiv.org/content/10.1101/2020.04.06.025635v1>

Smith CL, Blake JA, Kadin JA, Richardson JE, Bult CJ, Mouse Genome Database (MGD)-2018: Knowledgebase for the laboratory mouse. *Nucleic Acids Res.* (2018),

Subramanian A et al., Gene set enrichment analysis: A knowledge-based approach for interpreting genome-wide expression profiles. *Proc. Natl. Acad. Sci.* (2005),

Taiaroa G, Rawlinson D, Featherstone L, Pitt M, Caly L, Druce J, Purcell D, Harty L, Tran T, Roberts J, Catton M, Williamson D, Coin L, Duchene S. Direct RNA sequencing and early evolution 2 of SARS-CoV-2. 2020 Mar 7. *BioRxiv.* <https://www.biorxiv.org/content/10.1101/2020.03.05.976167v1>

Tang X, Wu C, Li X, Song Y, Yao X, Wu X, Duan Y, Zhang H, Wang Y, Qian Z, Cui J, Lu J. On the origin and continuing evolution of SARS-CoV-2, *National Science Review.* 2020. Mar 3.

Tanner NA, Zhang Y, Evans TC. Visual Detection of Isothermal Nucleic Acid Amplification Using pH-Sensitive Dyes. *Biotechniques.* 58 (2), 59-68. 2015 Feb 1.

van Doremalen N, Bushmaker T, Morris D, Holbrook M, Gamble A, Williamson B, Tamin A, Harcourt J, Thornburg N, Gerber S, Lloyd-Smith J, de Wit E, Munster V. Aerosol and surface stability of HCoV-19 (SARS-CoV-2) compared to SARS-CoV-1. 2020. Mar 17. *New England Journal of Medicine.*

Wang L, Wang S, Li W, RSeQC: Quality control of RNA-seq experiments. *Bioinformatics* (2012)

Woelfel R, Corman VM, Guggemos W, Seilmaier M, Zange S, Müller MA, Niemeyer D, Kelly TCJ, Vollmar P, Rothe C, Hoelscher M, Bleicker T, Brünink S, Schneider J, Ehmann R, Zwirgmaier K, Drosten C, Wendtner C. Virological assessment of hospitalized cases of coronavirus disease 2019 . 2020. Mar 8.

<https://www.medrxiv.org/content/10.1101/2020.03.05.20030502v1>

Wood DE, Lu J, Langmead B. Improved metagenomic analysis with Kraken 2. *Genome Biol.* (2019).

Yu G. Using ggtree to visualize data on tree-like structures. *Current Protocols in Bioinformatics*, 2020, 69:e96. doi: 10.1002/cpbi.96.

Yu L, Wu S, Hao X, Li X, Liu X, Ye S, Han H, Dong X, Li X, Li J, Liu J, Zhang W, Pelechano V, Chen W, Yin X. Rapid Colorimetric Detection of COVID-19 Coronavirus Using a Reverse Transcriptional Loop-Mediated Isothermal Amplification (RT-LAMP) Diagnostic Platform: iLACO. 2020 Feb 24.

<https://www.medrxiv.org/content/10.1101/2020.02.20.20025874v1>

Zamani S et al., *Mycobacterium avium* subsp. *paratuberculosis* and associated risk factors for inflammatory bowel disease in Iranian patients. *Gut Pathog.* 9, 1 (2017).

Zhao Z, Sokhansanj BA, Rosen G. Characterizing geographical and temporal dynamics of novel coronavirus SARS-CoV-2 using informative subtype markers. *BioRxiv*

<https://www.biorxiv.org/content/10.1101/2020.04.07.030759v3>

Zhang Y, Odiwuor N, Xiong J, Sun L, Nyaruaba RO, Wei H, Tanner NA. Rapid Molecular Detection of SARS-CoV-2 (COVID-19) Virus RNA Using Colorimetric LAMP. 2020. Feb 29.

MedRxiv <https://www.medrxiv.org/content/10.1101/2020.02.26.20028373v1>

Zhou F, Yu T, Du R, Fan G, Liu Y, Liu Z, Xiang J, Wang Y, Song B, Gu X, Guan L, Wei Y, Li H, Wu X, Xu J, Tu S, Zhang Y, Chen H, Cao B. Clinical course and risk factors for mortality of adult inpatients with COVID-19 in Wuhan, China: a retrospective cohort study. *Lancet.* 2020 Mar 11.

Figures and Legends

Butler, Mozsary, Meydan, Danko, Foox *et al.*, Host, Viral, and Environmental Transcriptome Profiles of the Severe Acute Respiratory Syndrome Coronavirus 2 (SARS-CoV-2)

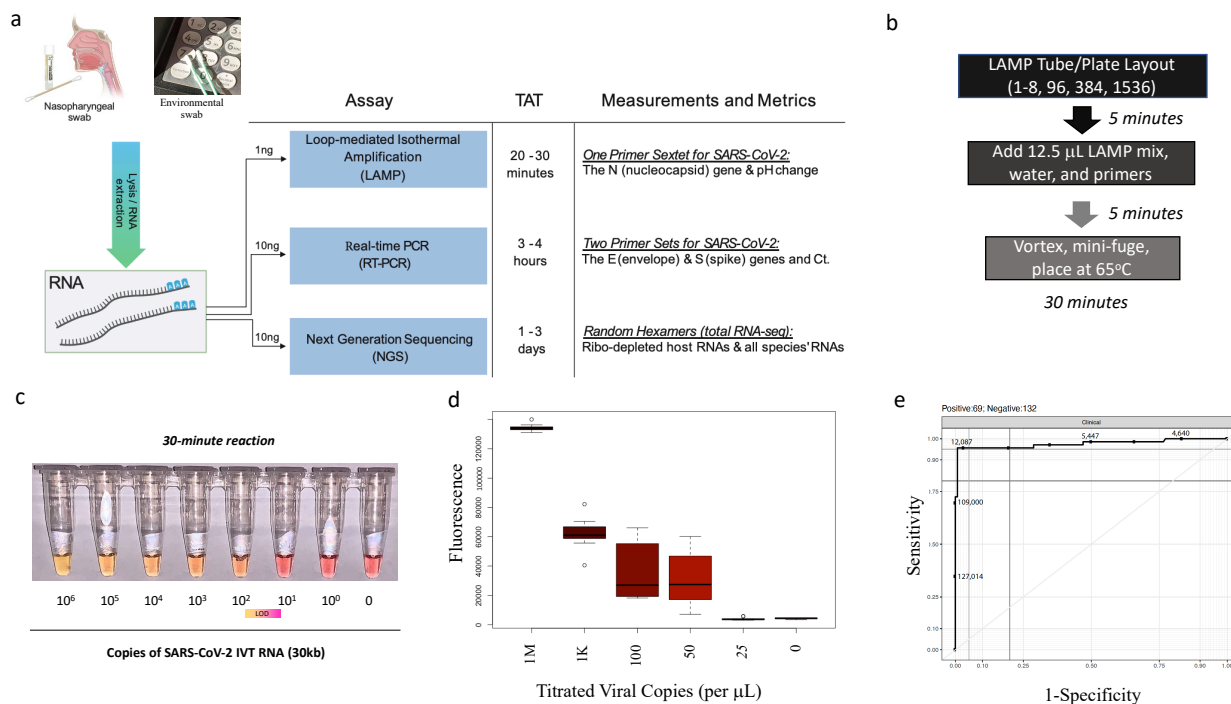


Figure 1. Sample Processing, the Loop-Mediated Isothermal (LAMP) Reaction and Synthetic RNA Validation. (A) Clinical and environmental samples collected with Nasopharyngeal (NP) and isohelix swabs respectively, were tested with RNA-sequencing, qRT-PCR, and LAMP. (B) The test samples were prepared using an optimized LAMP protocol from NEB, with a reaction time of 30 minutes. (C) Reaction progress was measured for the Twist COVID-19 synthetic RNA (*MT007544.1*) from 1 million molecules of virus (10^6), then titrated down by \log_{10} dilutions. The colorimetric findings of the LAMP assay are based on a yellow to pink gradient with higher copies of SARS-CoV-2 RNA corresponding to a yellow color. The limit of detection (LoD) range is shown with a gradient after 30 minutes between 10 and 100 viral copies (lower right). (D) Replicates of the titrated viral copies using LAMP, as measured by Quantifluor fluorescence. (E) The sensitivity and specificity of the LAMP assay from 201 patients (132 negative and 69 positive for SARS-CoV-2, as measured by qRT-PCR). Thresholds are DNA quantified by the Quantifluor.

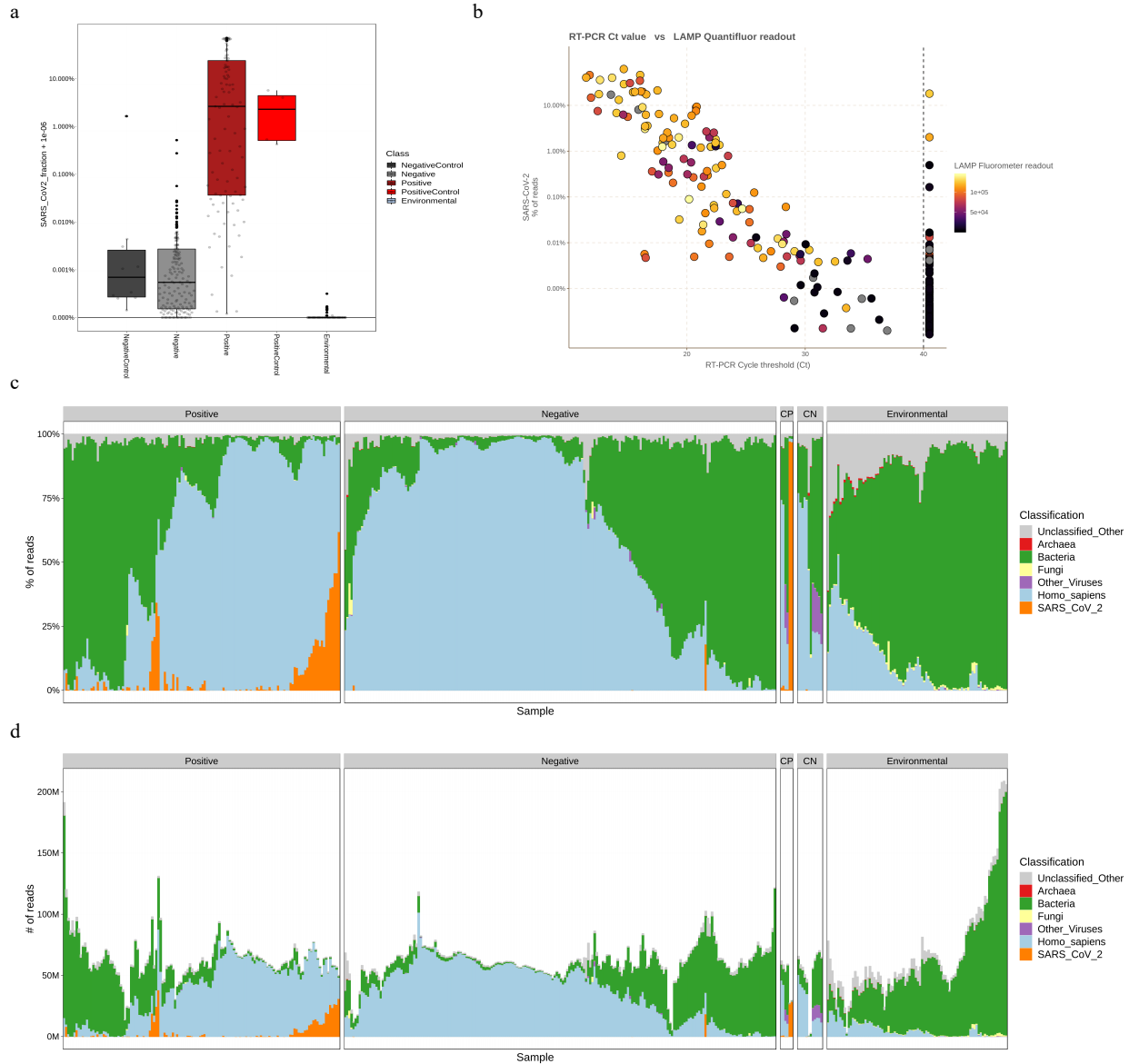


Figure 2. Full transcriptome profiles of SARS-CoV-2 Patients with NGS, qRT-PCR, and LAMP. (a) Clinical samples tested by qRT-PCR (Positive, dark red or Negative, light grey) were sequenced and run through the LAMP assay. These results were compared to the buffer blanks (Negative Control), dark grey, Synthetic RNAs or Vero 6 cell extracts with SARS-CoV-2 infection (Positive Controls, light red), and Subway Samples (Environmental, blue). Read proportions are shown on the y-axis. (b) SARS-CoV-2 abundance, as measured with NGS and percentage of reads (y-axis) is compared to the Ct Threshold for qRT-PCR (x-axis), with lower Ct values representing higher viral abundance, and the LAMP reaction output (Fluorimeter values, black to yellow scale). (c,d) Read mapping to archaea (red), bacteria (green), fungi (yellow), human (blue), and SARS-CoV-2 (orange), and other viruses (grey), across the clinical controls (CN, CP), environmental samples, qRT-PCR negative, and qRT-PCR positive samples.

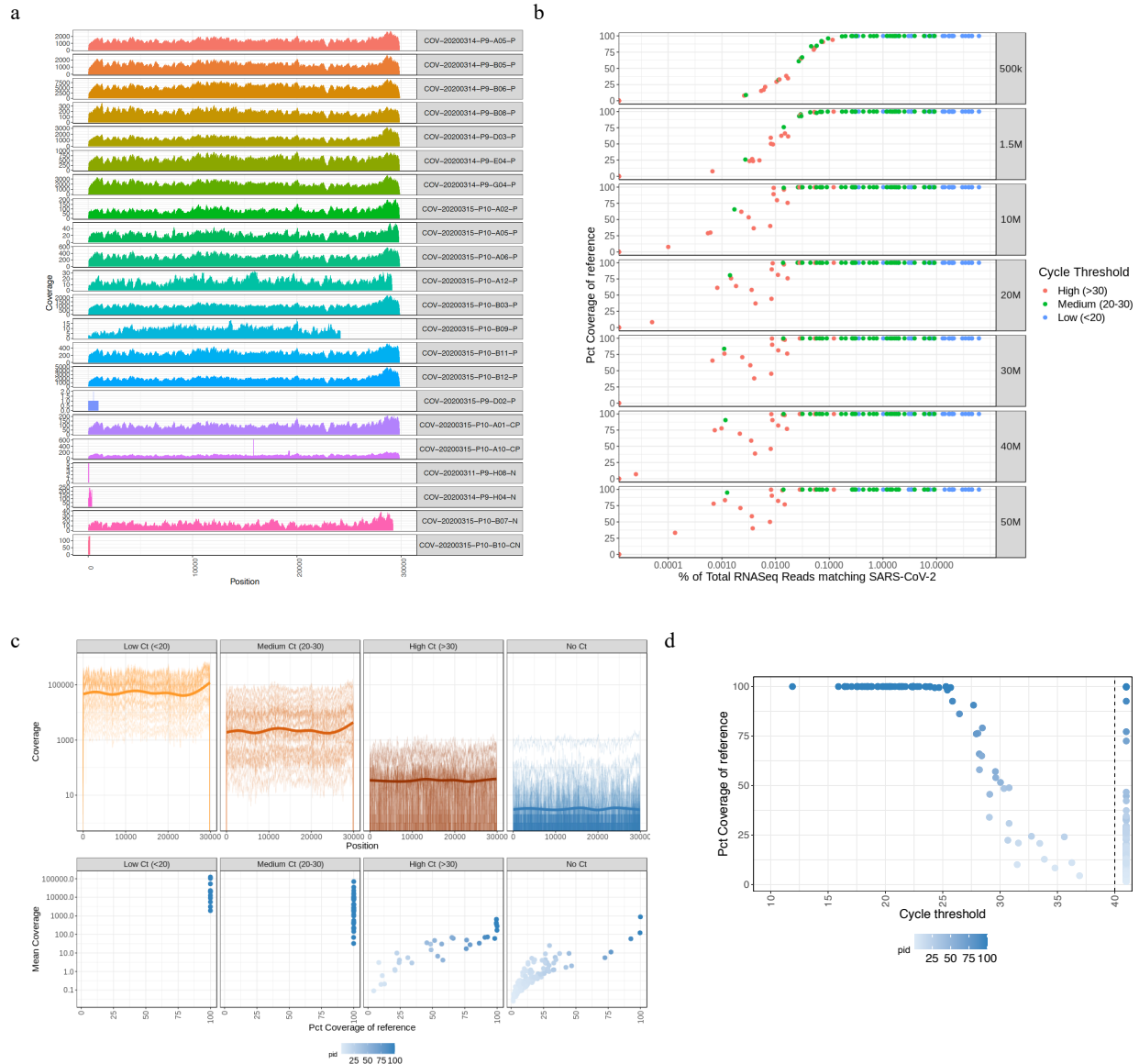


Figure 3: Viral genomes from RNA-seq data and titration of coverage (a) The coverage plot across the SARS-CoV-2 genomes (viral coordinate on bottom, colored by sample) from a representative set of clinical positive samples. Sample names with the suffixes CN and N are clinical negative (buffer), P are qRT-PCR positive, and CP are Vero 6 cells with virus. (b) Downsampling (right annotation) of the samples and mapping to the SARS-CoV-2 genome to gauge the percent coverage (y-axis) as a function of the viral quantification by qRT-PCR (Ct thresholds, low <20, medium 20-30, and high >30). (c) Average coverage statistics for the low, medium, and high Ct samples, as well as the mean coverage for each of these samples. (d) The cycle threshold (x-axis) vs. the coverage of the genome (y-axis and color depth) for the total RNA-seq.

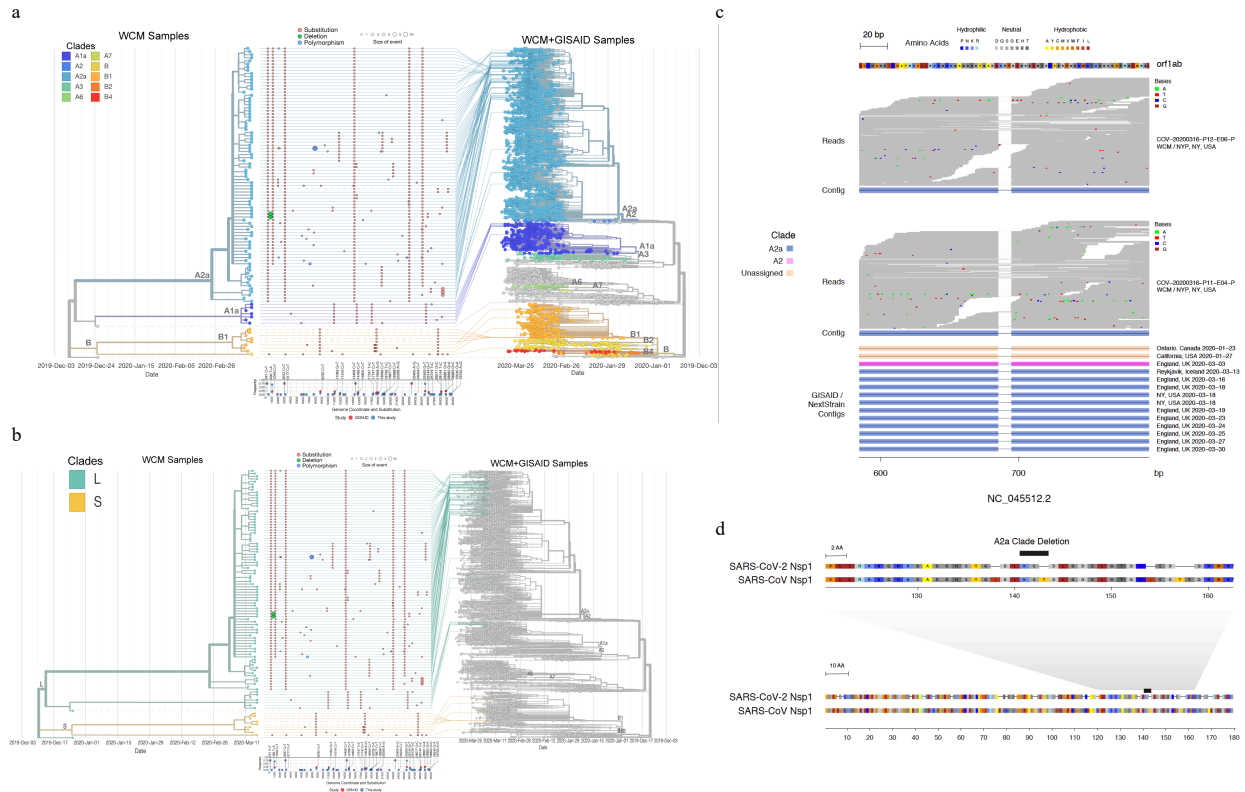


Figure 4: Variation and phylogenetics of NYC COVID-19 Cases. (a) The phylogenetic placement of these COVID samples is shown on the tree (left) and the global map of known COVID genomes (right). Genetic variants called from the RNA-seq data show a range of variants that are distinct from the Wuhan reference strain, and the samples from this study, highlighted in blue, show enrichment for European and Asian alleles. (b) Proportion of the L (green) and S strain (yellow) are shown for the NYC viruses. Phylogeny of samples from this study on the left and total GISAID samples on the right, with a map of variants in this study's samples in the middle, colored by event type and sized by number of nucleotides impacted. Annotation track on the bottom shows frequency of alternate alleles in this study and in the GISAID database. (c) The 9-bp deletion in ORF1b (NSP1) that was detected in samples from two patients was confirmed in the GISAID database (below). (d) Comparison of the ORF1b of the SARS-CoV-2 and SARS-CoV genomes with the 9-bp deletion region shown enlarged.

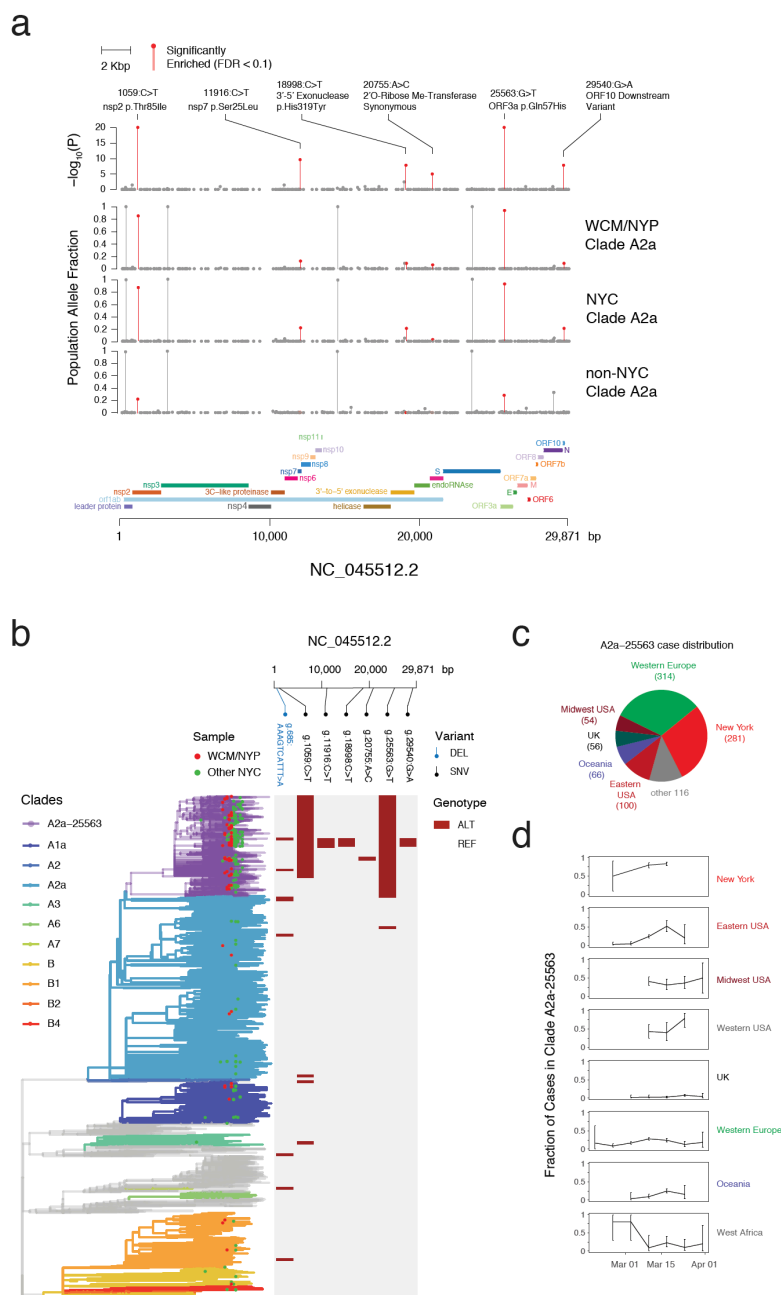


Figure 5: Variant and Subclade Analysis. (a) Six variant alleles were found to be significantly enriched by population allelic fraction within this set of 93 WCM/NYP cases as compared with non-NYC strains of Nextstrain clade A2a (1059:C>T $P = 6.26e^{-22}$, 11916:C>T $P = 3.09e^{-9}$, 18998:C>T $P = 2.51e^{-7}$, 20755:A>C $P = 1.32e^{-4}$, 25563:G>T $P = 9.6e^{-23}$, 29540:G>A $P = 2.51e^{-7}$). These variants demonstrated similar PAF enrichment within all other NYC strains as compared to non-NYC clade A2a (1059:C>T $P = 4.35e^{-84}$, 11916:C>T $P = 2.16e^{-43}$, 18998:C>T $P = 1.34e^{-25}$, 20755:A>C $P = 1.67e^{-4}$, 25563:G>T $P = 2.60e^{-83}$, 29540:G>A $P = 1.34e^{-46}$). (b) (left) Phylogenetic tree produced by the Nextstrain analysis with clade affiliations and nodes corresponding to WCM/NYP in red and other NYC cases in green. (right) occurrence of the six NYC-enriched alleles and the 9 nucleotide deletion across genomes. (c) Raw counts of cases present within this A2a-25563 subclade demonstrated a predominance of European and North American cases, with Western Europe and New York together comprising the majority of strains.

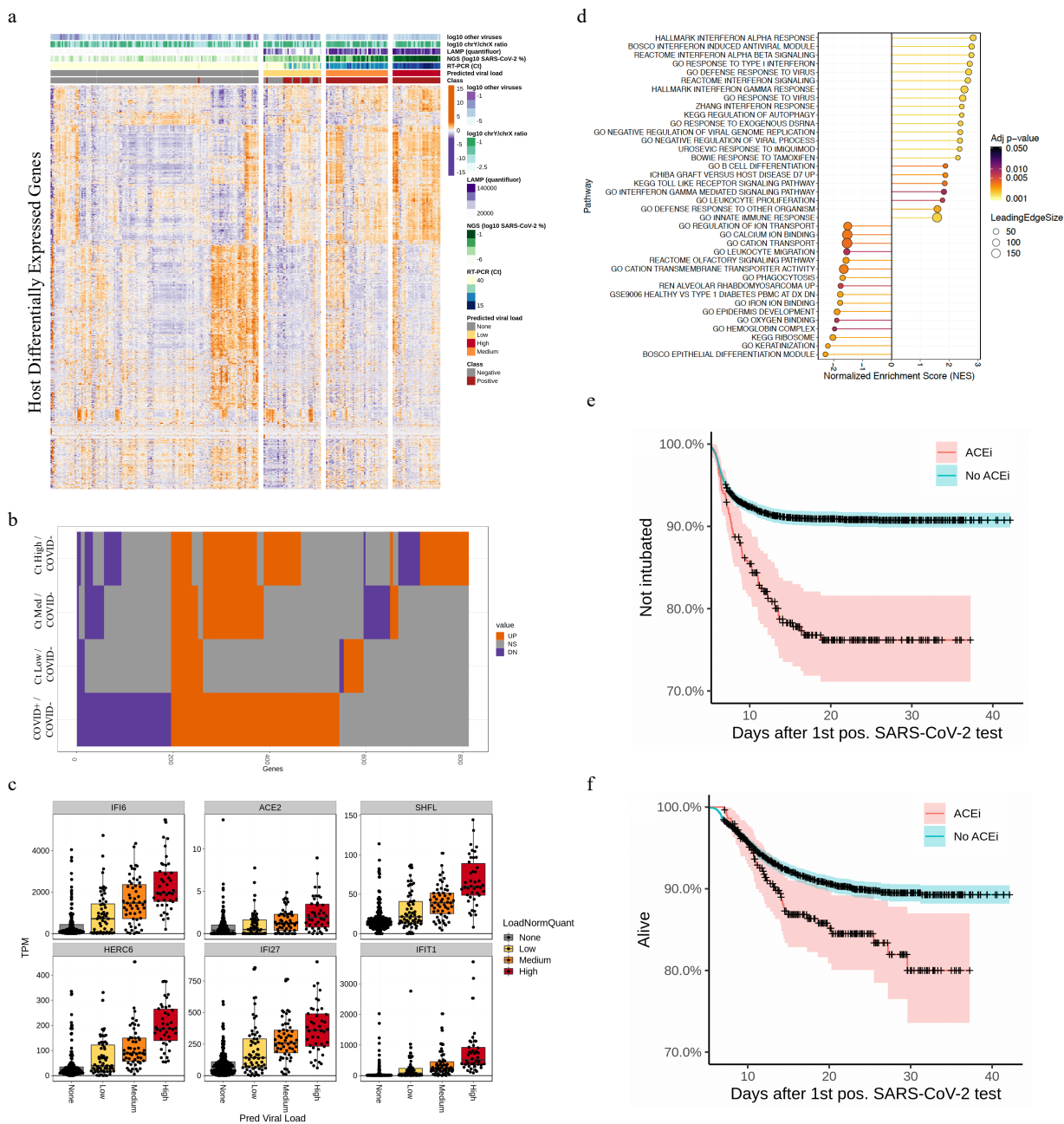


Figure 6: Host transcriptome responses and risk to SARS-CoV-2. (top row) Samples were quantified by a range of viral detection methods, including LAMP (Quantifluor), RNA-seq (log₁₀ SARS-CoV-2 % of reads), and qRT-PCR (Ct values) to create a three-tier range of viral load for the positive samples (right) compared to the clinically-annotated negative samples (class, red or grey). (bottom) The differentially expressed genes of COVID+ patients compared to COVID- patients showed up-regulated (orange) genes as well as down-regulated (purple) genes. (b) Up-regulated genes, with boxplots across all samples, include IFI6, ACE2, SHFL, HERC6, IFI27, and IFIT1, based on data from (c), which is the total set of DEGs. The full set is shown in an intersecting heat map, with a core set of up-regulated genes (orange) distinct from the set of down-regulated genes (purple), compared to genes that are not significantly differently

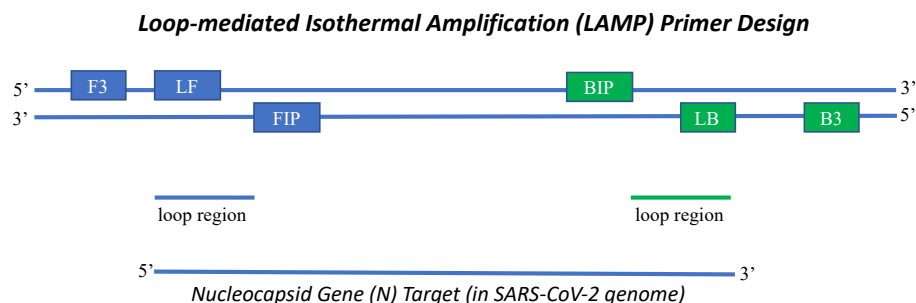
expressed (grey) in any comparison (DESeq2, q-value <0.01, |logFC| >0.58). (d) Significantly different gene ontology (GO) pathways between COVID-POS and COVID-NEG patients include interferon response and host response to infection, as well as some ion and heme transport mechanisms. (e) Survival curves for requiring mechanical respiration (identified by intubation procedure notes) (e) and mortality (f). Patients with a history of ACE inhibitor exposure were more likely to require intubation (HR=2.63 95%CI 2.01-3.43, p=1.22E-12; (e) and less likely to survive (HR=1.68 95%CI: 1.22-2.31, p=1.42E-03; (f). Because several individuals were intubated shortly before they first tested positive for SARS-CoV-2 infection, each first positive test was set back by seven days to account for testing delays.

Table 1. Baseline characteristics of SARS-CoV-2 suspected cohort. General population refers to a comparison cohort of individuals administered drugs at NYP/CUIMC in 2019 who were not later tested for SARS-COV-2 infection.

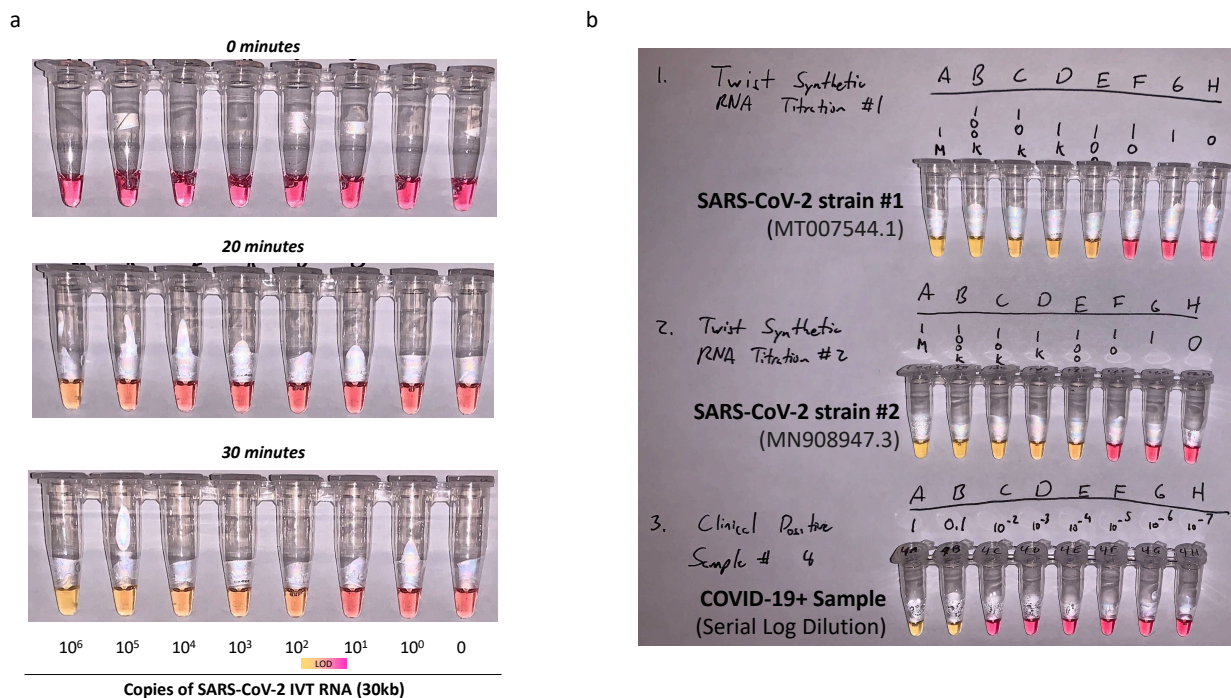
	General Population	Tested	COV+	COV+/Intubated	COV+/Died
N (% of tested)	279487	8278 (100%)	4574 (55.3%)	493 (6%)	423 (5.1%)
ACEi	20017 (7.2%)	370 (4.5%)	290 (6.3%)	69 (14%)	42 (9.9%)
Median age (95%)	28.8 (1.4-49.3)	55.7 (0.5-91.3)	62.1 (23.3-92.5)	65.1 (19.3-89.3)	79.2 (49-96.1)
Male	118555 (42.4%)	3806 (46%)	2413 (52.8%)	308 (62.5%)	251 (59.3%)
Black/ African-American	80449 (28.8%)	917 (11.1%)	531 (11.6%)	71 (14.4%)	59 (13.9%)
Caucasian	24267 (8.7%)	1392 (16.8%)	682 (14.9%)	89 (18.1%)	89 (21%)
Asian or Pacific Islander	9 (0.003%)	88 (1.1%)	30 (0.7%)	3 (0.6%)	2 (0.5%)
Other race	167 (0.06%)	1934 (23.4%)	1170 (25.6%)	165 (33.5%)	164 (38.8%)
Missing race	174595 (62.5%)	3947 (47.7%)	2161 (47.2%)	165 (33.5%)	109 (25.8%)
Hispanic/Latino	36905 (13.2%)	1750 (21.1%)	1088 (23.8%)	171 (34.7%)	159 (37.6%)
Non-Hispanic/Latino	87562 (31.3%)	1547 (18.7%)	746 (16.3%)	85 (17.2%)	87 (20.6%)
Other listed ethnicity	155020 (55.5%)	1034 (12.5%)	579 (12.7%)	72 (14.6%)	68 (16.1%)
Hypertension	104925 (38.4%)	2168 (26.2%)	1368 (29.9%)	221 (44.8%)	260 (61.5%)
CAD/CHD	155561 (56.9%)	816 (9.9%)	503 (11%)	84 (17%)	115 (27.2%)

Diabetes	46908 (17.2%)	1274 (15.4%)	834 (18.2%)	151 (30.6%)	174 (41.1%)
Overweight	39192 (14.3%)	452 (5.5%)	259 (5.7%)	43 (8.7%)	38 (9%)
No risk factors	110460 (40.4%)	5830 (70.4%)	3052 (66.7%)	248 (50.3%)	150 (35.5%)
Median IL-6 (50%)	-	30.6 (8-94.1)	31.1 (8-94.9)	68.2 (16-178)	68 (18-153.8)

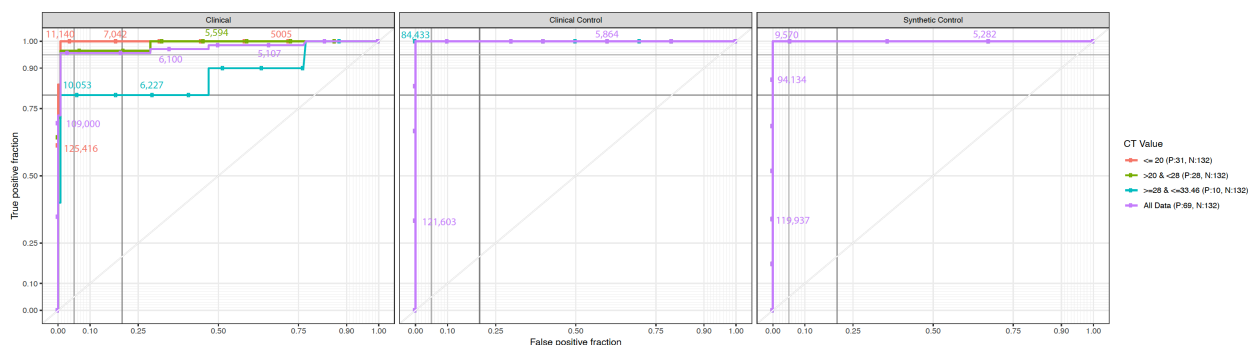
Supplemental Figures



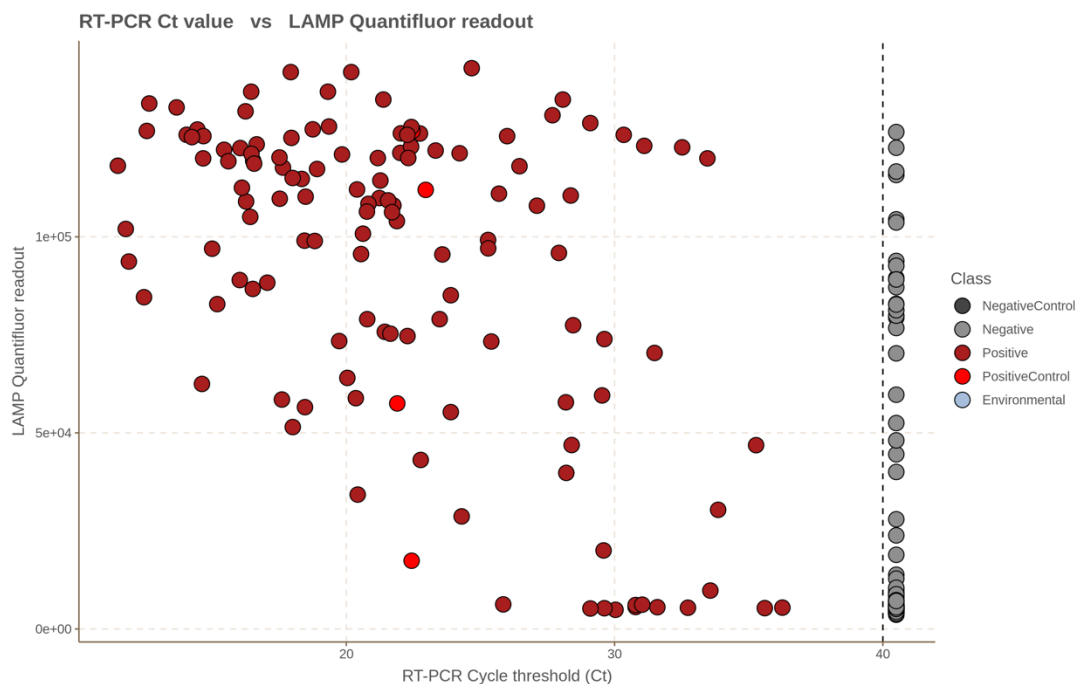
Supplemental Figure 1: LAMP Primer Design. PrimerDesigner (v4) was used to create a set of six primers that would specifically target the nucleocapsid gene (N) in the COVID-19 genome. Primer sequences are listed in the methods section.



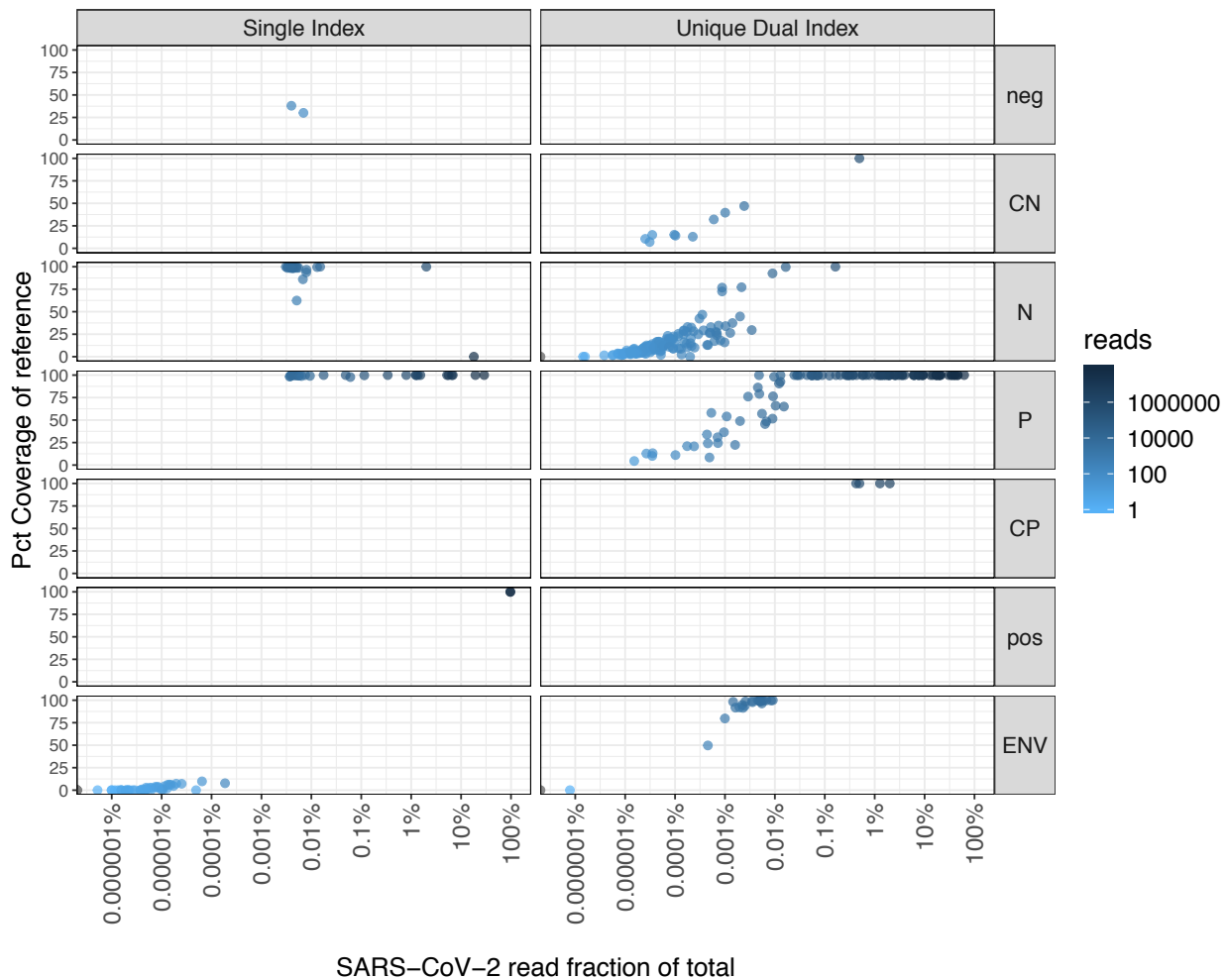
Supplemental Figure 2. Additional Testing and Titration of the LAMP Assay with Synthetic and Clinical Samples. Samples were prepared using the LAMP protocol with a reaction time of 30 minutes. Reaction progress was measured (a) from 0, 20, and 30 minutes. (b) This was repeated for both Twist COVID-19 synthetic RNAs (*MT007544.1*, top and *MN908947.3*, middle) from 1 million molecules of virus (10⁶), then titrated down by log₁₀ dilutions. Limit of Detection (LOD) range is shown with a gradient after 30 minutes between 10 and 100 viral copies. (bottom) A clinically positive sample that was not detectable by Qubit (<0.05 ng/mL) was nonetheless detected by LAMP, in accordance with detection of low viral titer samples.



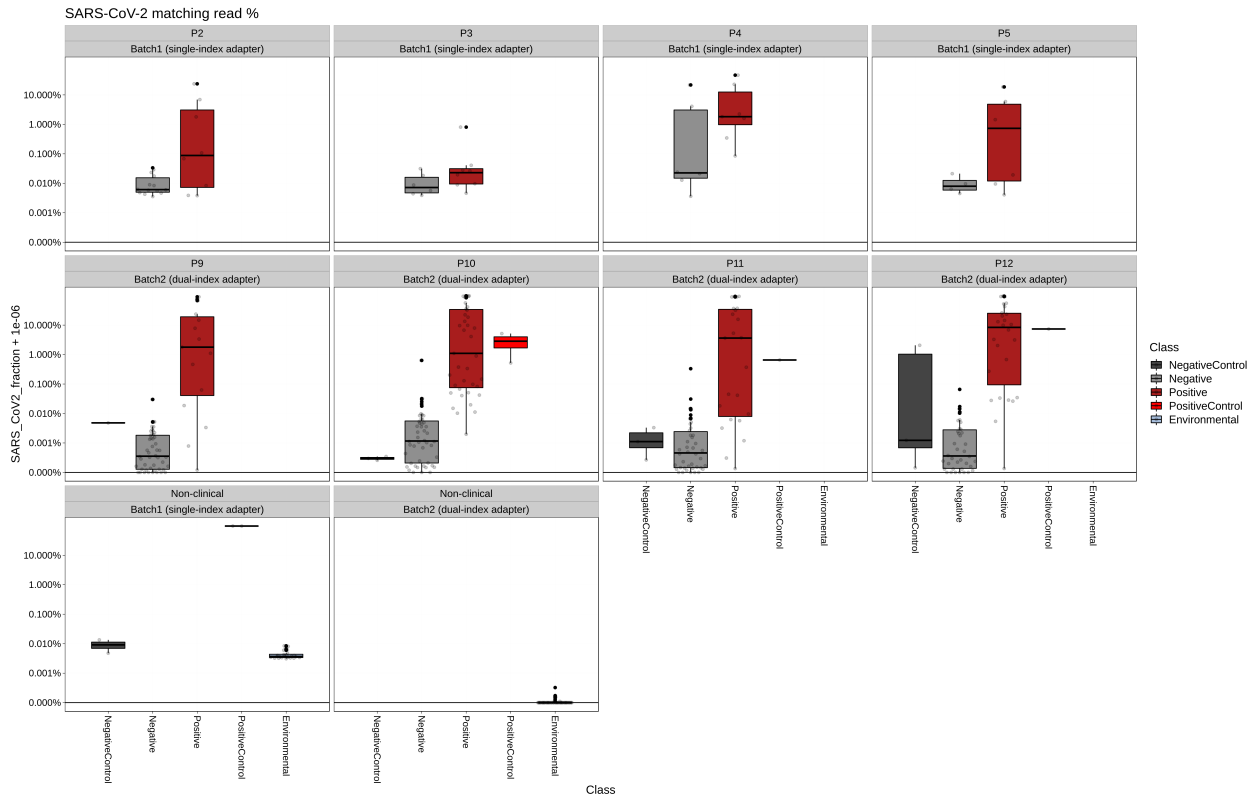
Supplemental Figure 4. Ct and RFU (Relative Fluorescence Units) Thresholds for the LAMP Assay. With increasing viral load, as measured by qRT-PCR, the LAMP assay shows an increased sensitivity (y-axis) and specificity (y-axis). For high and medium viral count samples (Ct < 28, red and green line), we see 100% sensitivity, and for low viral count, we see 81% sensitivity and 100% specificity (blue). Across all data (purple), we see 95.6% sensitivity and 99.4% specificity. RFU thresholds are shown as numbers.



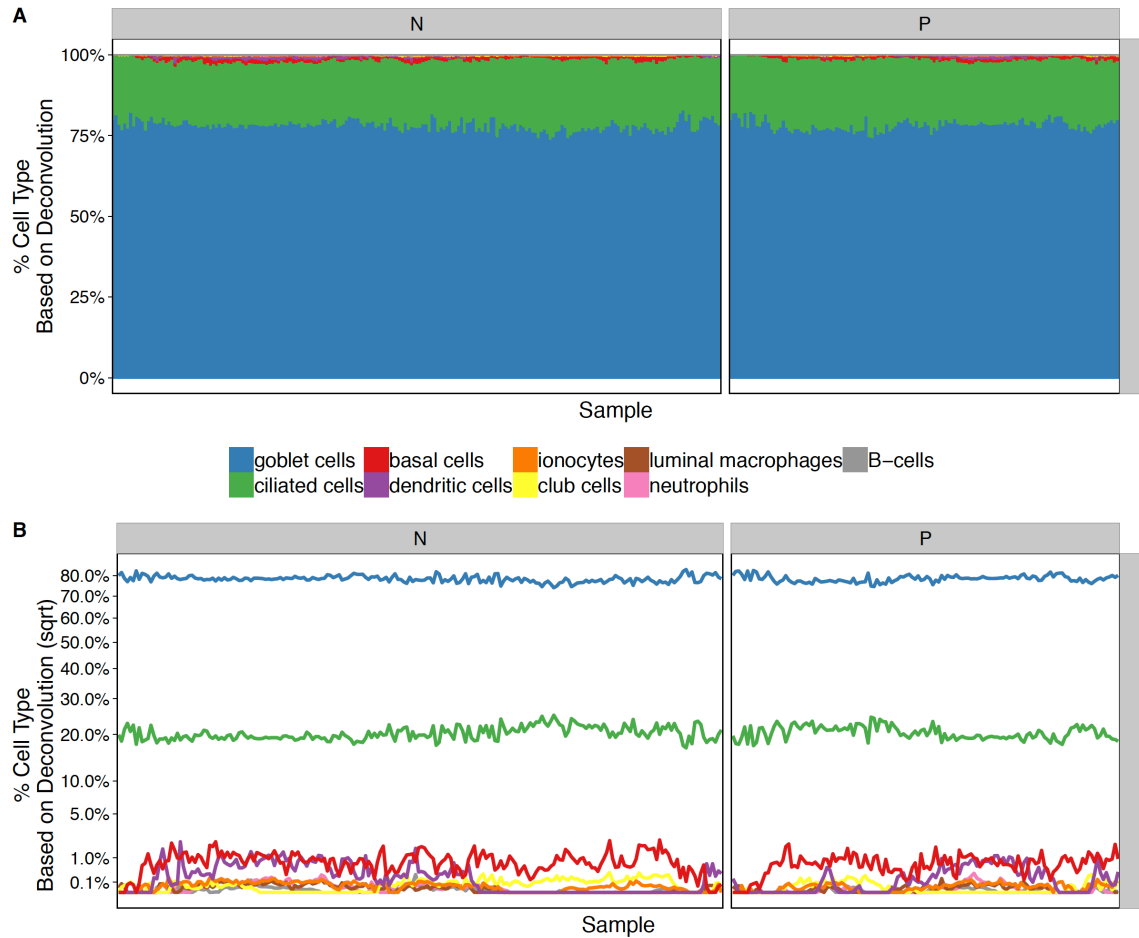
Supplementary Figure 5. Correlation between LAMP Reaction Output and qRT-PCR. Clinical samples tested by qRT-PCR (Positive, dark red or Negative, light grey) were run with the LAMP assay and compared to the buffer blanks (Negative Control), dark grey, Synthetic RNAs or Vero 6 cell extracts with SARS-CoV-2 infection (Positive Controls, light red), and Subway Samples (Environmental, blue, lower right). The DNA abundance, as measured with the GloMax Quantifluor (y-axis) is compared to the Ct Threshold for qRT-PCR (x-axis), with lower Ct values representing higher viral abundance.



Supplementary Figure 6. Coverage of COVID samples by Index and Sample Type. Clinical samples tested by qRT-PCR (Positive, P, Negative, N) were compared to the buffer blanks (Negative Control, N and neg), Synthetic RNAs or Vero 6 cell extracts with SARS-CoV-2 infection (CP and pos) and Subway Samples (Environmental, ENV). The %identity to the SARS-CoV-2 reference (y-axis) is shown relative to the proportion of reads that mapped from NGS (x-axis). The unique, dual-index runs (left panels) are shown relative to the single-index runs (right panels). The initial set of single-index libraries were associated with a non-negligible background of viral load in clinical negative samples, this effect was eliminated with the dual-indexing approach for all remaining samples.

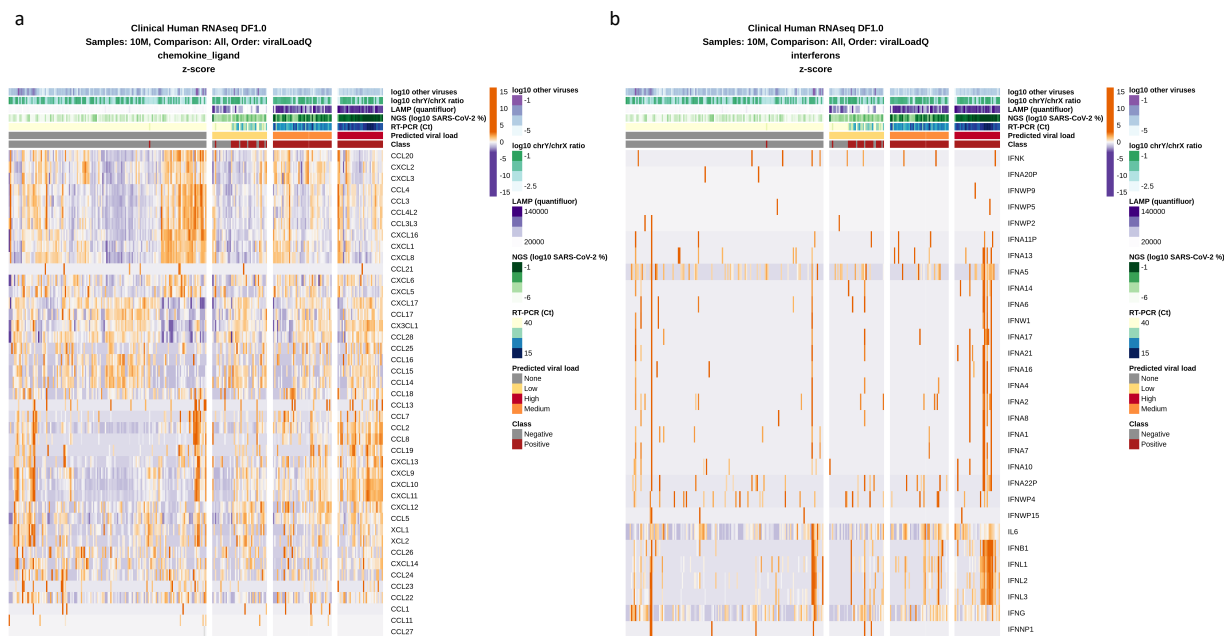


Supplemental Figure 8. Proportion of RNA-seq reads mapping SARS-CoV-2. Clinical samples tested by qRT-PCR (Positive, dark red or Negative, light grey) were sequenced and compared to the buffer blanks (Negative Control), dark grey, Synthetic RNAs or Vero 6 cell extracts with SARS-CoV-2 infection (Positive Controls, light red), and Subway Samples (Environmental, blue). Read totals are shown on the y-axis. Differences between single index barcodes are plotted across each of the plates of samples that were processed.

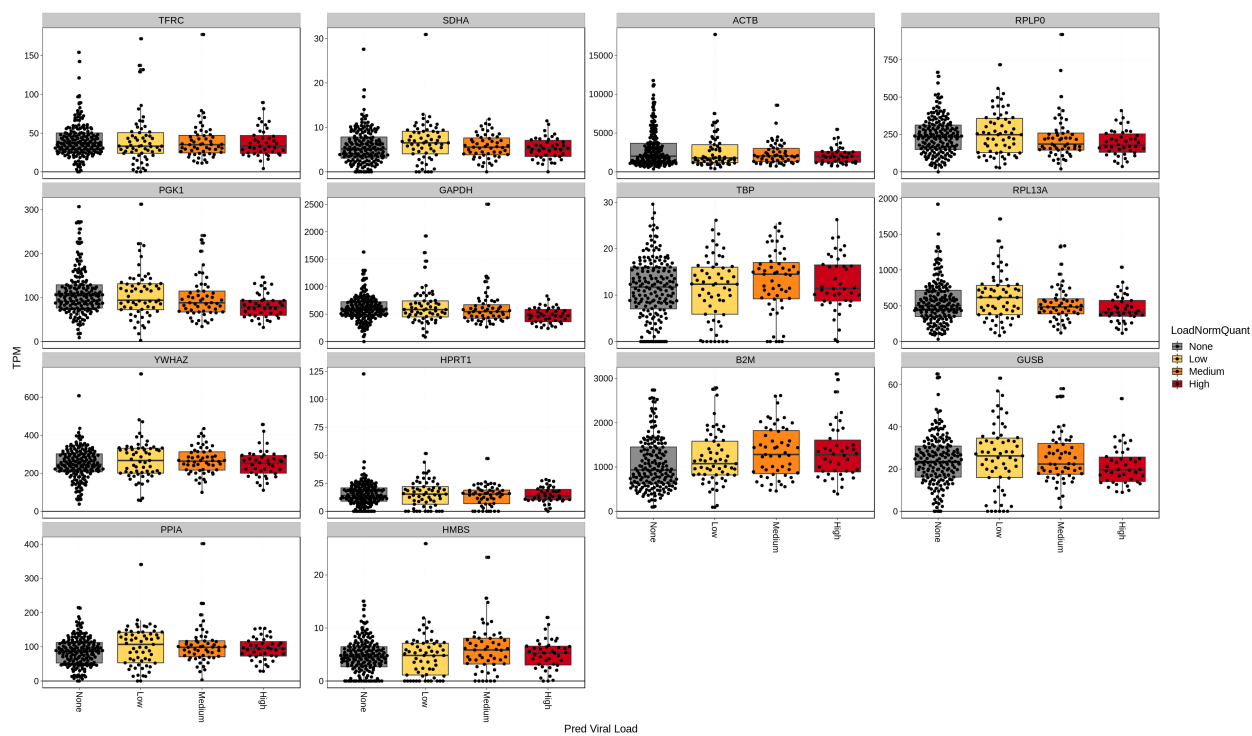


Supplemental Figure 9. Cellular sub-type deconvolution from nasopharyngeal (NP) swabs.

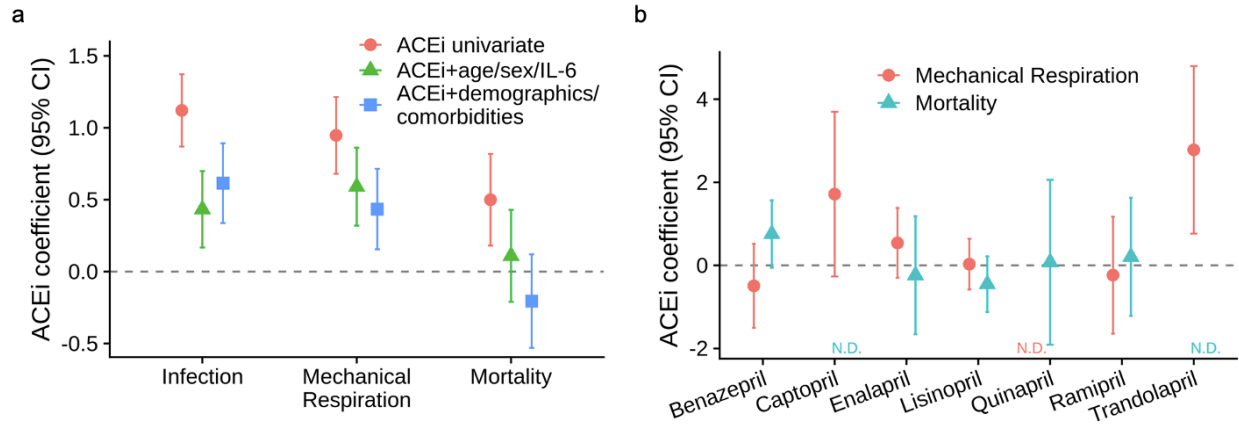
The Bisque algorithm (<https://github.com/cozygene/bisque>) was used to separate the cellular sub-type gene expression signatures present in the total RNA-seq data from the NP swabs. (a) The fraction of cells estimated for each cell type (y-axis) was calculated for the samples that tested positive by RT-qPCR (P, positive on the right) as well as negative by RT-qPCR (N, negative on the left), with proportions shown for goblet cells (blue), ciliated cells (green), basal cells (red), dendritic cells (purple), ionocytes (orange), club cells (yellow), luminal macrophages (brown), neutrophils (pink), and B-cells (grey). (b) The same data is in (a) shown as the square root for visibility of low incidence cell types.



Supplemental Figure 10. Cytokine and interferon profiles of the host transcriptome. Top rows: samples were quantified by a range of viral detection methods, including LAMP (Quantifluor), RNA-seq (log10 SARS-CoV-2 % of reads), and qRT-PCR (Ct values) to create a three-tier range of viral load for the positive samples (right) compared to the clinically-annotated negative samples (class, red or grey). (bottom) The differentially expressed genes of COVID+ patients compared to COVID- patients showed up-regulated (orange) genes as well as down-regulated (purple) genes. (a) Chemokine profiles for the samples (x-axis) is plotted for each related gene (y-axis), and the same plotting function shows in (b) the interferon and interleukin gene profiles of IL6.



Supplemental Figure 11. Housekeeping host genes relative to SARS-CoV-2 infection. Clinical samples were sequenced with RNA-seq and quantified to a set of genes for their expression levels. Samples with no virus (grey) were compared to those with low (yellow), medium (orange), and high (red) expression levels, based on qRT-PCR.



Supplemental Figure 12. ACEI Multivariate and Comparative Analyses. (a) Regression coefficients for variables indicating exposure/history of exposure to ACE inhibitors for each of the three cohort comparisons: (left) test outcome in a cohort of patients suspected of SARS-CoV-2 infection, (middle) requirement of mechanical respiration in patients who tested positive, (right) mortality in patients who tested positive. Univariate analyses are shown as red circles. The green triangles coefficients are when correcting for age, sex, and baseline IL-6 levels take upon admission. The blue squares are from a model that includes age, sex, and IL-6 as well as comorbidities including CAD/CHD, diabetes, obesity, and self-reported race and ethnicity. (b) Comparison of the effects of different ACE inhibitors. We directly compared the effects of specific ACE inhibitors among those patients with evidence of exposure to ACE inhibitors. We found two significant associations: benazepril was significantly associated with higher mortality (HR=2.37 95%CI 1.05-5.35, $p=3.70E-02$) and trandolapril was associated with requirement of mechanical ventilation (HR=15.85 95% CI: 2.11-119.08, $p=7.25E-03$). N.D. indicates that a result was not displayed due to low sample size and, therefore, very large errors.

Supplementary Table 1: Metatranscriptome Profiles of All Samples. Appended.

Supplementary Table 2: Taxonomic Mis-assignment Filter. The entire SARS-CoV-2 genome was fragmented (wgsim) and then re-mapping to the entire Kraken2 database. These species were then used to flag putative false positives from SARS-CoV-2 genome segments that are similar to other organisms.

Supplementary Table 2 : Other Taxonomic Alignments for SARS-CoV-2 (High-risk false positives)		
Taxonomic group (domain, phylum, class, order, family, genus, species, strain)	TaxonName	% match
d_Viruso_Nidoviralesf_Coronaviridae_Betacoronavirus_Severe acute respiratory syndrome-related coronavirus	Severe acute respiratory syndrome-related coronavirus (SARS)	95.0813%
d_Viruso_Nidoviralesf_Coronaviridae_Bat coronavirus BM48-31/BGR/2008	Bat coronavirus BM48-31/BGR/2008	0.3937%
d_Eukaryotak_Metazoap_ChordataM_Mammaliao_Primatef_HominidaeH_HomoH_Homo sapiens	Homo sapiens	0.0170%
d_Viruso_Nidoviralesf_Coronaviridae_Alphacoronavirus_Rhinolophus ferrumequinum alphacoronavirus HuB-2013	Rhinolophus ferrumequinum alphacoronavirus HuB-2013	0.0164%
d_Viruso_Nidoviralesf_Coronaviridae_Betacoronavirus_Betacoronavirus 1	Betacoronavirus 1	0.0099%
d_Viruso_Nidoviralesf_Coronaviridae_Betacoronavirus_Murine coronavirus	Murine coronavirus	0.0089%
d_Viruso_Nidoviralesf_Coronaviridae_Betacoronavirus_Rousettus bat coronavirus GCCDC1	Rousettus bat coronavirus GCCDC1	0.0059%
d_Viruso_Nidoviralesf_Coronaviridae_Bat coronavirus	Bat coronavirus	0.0049%
d_Bacteriap_FirmicutesC_ClostridiaO_Clostridialesf_ClostridiaceaeG_ClostridiumC_Clostridium botulinum	Clostridium botulinum	0.0045%
d_Bacteriap_FirmicutesC_ClostridiaO_Clostridialesf_ClostridiaceaeG_Clostridium perfringens	Clostridium perfringens	0.0037%
d_Bacteriap_FusobacteriiaF_Fusobacterialesf_FusobacteriaceaeG_FusobacteriumF_Fusobacterium varium	Fusobacterium varium	0.0027%
d_Viruso_Nidoviralesf_Coronaviridae_Alphacoronavirus_Myotis ricketti alphacoronavirus Sax-2011	Myotis ricketti alphacoronavirus Sax-2011	0.0025%
d_Bacteriap_ProteobacteriaC_GammaproteobacteriaO_Enterobacterialesf_ErwiniaC_Buchnera aphidicola	Buchnera aphidicola	0.0024%
d_Bacteriap_FirmicutesC_Bacillio_Bacillalesf_ThermoactinomycesC_ThermoactinomycetesS_Thermoactinomyces vulgaris	Thermoactinomyces vulgaris	0.0023%
d_Bacteriap_FirmicutesC_Bacillio_Lactobacillalesf_StreptococcaceaeG_StreptococcusS_Streptococcus pyogenes	Streptococcus pyogenes	0.0023%
d_Bacteriap_ProteobacteriaC_AlphaproteobacteriaO_Rickettsialesf_AnaplasmataceaeG_EhrlichiaS_Ehrlichia sp. HF	Ehrlichia sp. HF	0.0018%
d_Bacteriap_FirmicutesC_Bacillio_Bacillalesf_BacillaceaeG_BacillusS_Bacillus cereus	Bacillus cereus	0.0017%
d_Bacteriap_BacteroidetesC_BacteroidiaO_BacteroidalesG_Candidatus AzobacteroidesS_Candidatus Azobacteroides pseudotrichonymphae	Candidatus Azobacteroides pseudotrichonymphae	0.0017%
d_Viruso_Nidoviralesf_Coronaviridae_Betacoronavirus_Rousettus bat coronavirus HKU9	Rousettus bat coronavirus HKU9	0.0015%
d_Viruso_Behai picorna-like virus 116	Behai picorna-like virus 116	0.0015%
d_Bacteriap_ProteobacteriaC_EpsilonproteobacteriaO_Campylobacterialesf_HelicobacteriaceaeG_HelicobacterS_Helicobacter pylori	Helicobacter pylori	0.0014%
d_Bacteriap_ProteobacteriaC_BetaproteobacteriaO_Burkholderialesf_OxalobacteraceaeG_JanthinobacteriumS_Janthinobacterium sp. B9-8	Janthinobacterium sp. B9-8	0.0014%
d_Eukaryotap_ApicomplexaC_AconoidasidaO_HaemosporidaP_PlasmodiidaeG_PlasmodiumS_Plasmodium coatneyi	Plasmodium coatneyi	0.0014%
d_Bacteriap_ProteobacteriaC_GammaproteobacteriaO_Enterobacterialesf_YersiniaceaeG_SerratiaS_Serratia symbiotica	Serratia symbiotica	0.0013%
d_Bacteriap_ProteobacteriaC_GammaproteobacteriaO_Pseudomonadalesf_MoraxellaceaeG_AcinetobacterS_Acinetobacter baumannii	Acinetobacter baumannii	0.0013%
d_Bacteriap_FirmicutesC_ClostridiaO_Clostridialesf_ClostridiaceaeG_ClostridiumS_Clostridium septicum	Clostridium septicum	0.0013%
d_Viruso_Nidoviralesf_Coronaviridae_Betacoronavirus_Tylosynceris bat coronavirus HKU4	Tylosynceris bat coronavirus HKU4	0.0012%
d_Bacteriap_FirmicutesC_Bacillio_Bacillalesf_StaphylococcaceaeG_StaphylococcusS_Staphylococcus cohnii	Staphylococcus cohnii	0.0012%
d_Bacteriap_FirmicutesC_ClostridiaO_Clostridialesf_ClostridiaceaeG_CaloranaerobacterS_Caloranaerobacter azorensis	Caloranaerobacter azorensis	0.0012%
d_Bacteriap_CyanobacteriaO_Nostocalesf_CalothrixaceaeG_CalothrixS_Calothrix sp. NIES-2098	Calothrix sp. NIES-2098	0.0012%
d_Viruso_Nidoviralesf_Coronaviridae_Betacoronavirus_Bat Hp-betacoronavirus Zhejiang2013	Bat Hp-betacoronavirus Zhejiang2013	0.0011%
d_Bacteriap_ProteobacteriaC_GammaproteobacteriaO_Enterobacterialesf_ErwiniaC_Candidatus Erwinia haradaeae	Candidatus Erwinia haradaeae	0.0011%
d_Bacteriap_ProteobacteriaC_GammaproteobacteriaO_Thiotrichalesf_ThiotrichaceaeG_ThioplocaS_Thioploca ingrica	Thioploca ingrica	0.0011%
d_Bacteriap_ProteobacteriaC_AlphaproteobacteriaO_Rhodospirillalesf_AcetobacteraceaeG_BombellaS_Bombella sp. KACC 21507	Bombella sp. KACC 21507	0.0011%
d_Bacteriap_CyanobacteriaO_Chroococcalesf_AphanothecaceaeG_Candidatus AtelocyanobacteriumS_Candidatus Atelocyanobacterium thalassa	Candidatus Atelocyanobacterium thalassa	0.0011%
d_Bacteriap_ProteobacteriaC_GammaproteobacteriaO_Enterobacterialesf_ErwiniaC_WigglesworthiaS_Wigglesworthia glossinidia	Wigglesworthia glossinidia	0.0010%
d_Bacteriap_ProteobacteriaC_GammaproteobacteriaO_Enterobacterialesf_EnterobacteriaceaeG_EnterobacterS_Enterobacter hormaechei	Enterobacter hormaechei	0.0010%
d_Bacteriap_ProteobacteriaC_GammaproteobacteriaO_Alteromonadalesf_ColwelliaceaeG_ColwelliaS_Colwellia sp. PAMC 20917	Colwellia sp. PAMC 20917	0.0010%
d_Bacteriap_ProteobacteriaC_BetaproteobacteriaO_Neisserialesf_NeisseriaceaeG_NeisseriaS_Neisseria flavescens	Neisseria flavescens	0.0010%
d_Bacteriap_BacteroidetesC_FlavobacteriiaF_Flavobacterialesf_FlavobacteriaceaeG_LutibacterS_Lutibacter profundus	Lutibacter profundus	0.0010%

Supplementary Table 3: Differentially Expressed Genes in COVID-19+/- patients.
Appended.

Supplemental Table 4: Gene Ontology Pathways.
Appended

Supplementary Table 5: COVID-19 Rapid Colorimetric LAMP Detection Test: N Primers Specificity
Appended

Supplementary Table 6: GISAID COVID-19 Acknowledgments
Appended